ATLAS NOTE

ATLAS-CONF-2016-078

4th August 2016

Further searches for squarks and gluinos in final states with jets and missing transverse momentum at $\sqrt{s}$ =13 TeV with the ATLAS detector

The ATLAS Collaboration

Abstract

Two selection strategies to search for the supersymmetric partners of quarks and gluons (squarks and gluinos) in final states containing hadronic jets, missing transverse momentum but no electrons or muons are presented. The data used for both approaches were recorded in 2015 and 2016 by the ATLAS experiment in $\sqrt{s}$ = 13 TeV proton–proton collisions at the Large Hadron Collider, corresponding to an integrated luminosity of 13.3 fb^{-1}. The results are interpreted in the context of various simplified models where squarks and gluinos are pair-produced and the neutralino is the lightest supersymmetric particle. An exclusion limit at the 95% confidence level on the mass of the gluino is set at 1.86 TeV for a simplified model incorporating only a gluino octet and the lightest neutralino, assuming the lightest neutralino is massless. For a simplified model involving the strong production of mass-degenerate first- and second-generation squarks, squark masses below 1.35 TeV are excluded for a massless lightest neutralino. These limits substantially extend the region of supersymmetric parameter space excluded by previous measurements with the ATLAS detector.

ATLAS-CONF-2016-078
08 August 2016

1. Introduction

Supersymmetry (SUSY) [1–6] is a generalization of space-time symmetries that predicts new bosonic partners for the fermions and new fermionic partners for the bosons of the Standard Model (SM). If R-parity is conserved [7], SUSY particles (called sparticles) are produced in pairs and the lightest supersymmetric particle (LSP) is stable and represents a possible dark-matter candidate. The scalar partners of the left- and right-handed quarks, the squarks $\tilde{q}_{\mathrm{L}}$ and $\tilde{q}_{\mathrm{R}}$, mix to form two mass eigenstates $\tilde{q}_1$ and $\tilde{q}_2$ ordered by increasing mass. Superpartners of the charged and neutral electroweak and Higgs bosons also mix to produce charginos ($\tilde{\chi}^{\pm}$) and neutralinos ($\tilde{\chi}^{0}$). Squarks and the fermionic partners of the gluons, the gluinos ($\tilde{g}$), could be produced in strong-interaction processes at the Large Hadron Collider (LHC) [8] and decay via cascades ending with the stable LSP, which escapes the detector unseen, producing substantial missing transverse momentum ($\boldsymbol{E}_{\mathrm{T}}^{\mathrm{miss}}$).

The large expected cross-sections predicted for the strong production of supersymmetric particles make the production of gluinos and squarks the primary target for early searches for SUSY in proton–proton (pp) collisions at a centre-of-mass energy of 13 TeV at the LHC. Interest in these searches is motivated by the large number of R-parity-conserving models [9, 10] in which squarks (including anti-squarks) and gluinos can be produced in pairs ($\tilde{g}\tilde{g}$, $\tilde{q}\tilde{q}$, $\tilde{q}\tilde{g}$) and can decay through $\tilde{q} \to q\tilde{\chi}_1^0$ and $\tilde{g} \to q\bar{q}\tilde{\chi}_1^0$ to the lightest neutralino, $\tilde{\chi}_1^0$, assumed to be the LSP. Additional decay modes can include the production of charginos via $\tilde{q} \to q\tilde{\chi}^{\pm}$ (where $\tilde{q}$ and q are of different flavour) and $\tilde{g} \to q\bar{q}\tilde{\chi}^{\pm}$, or neutralinos via $\tilde{g} \to q\bar{q}\tilde{\chi}_2^0$. Subsequent chargino decay to $W^{\pm}\tilde{\chi}_1^0$ or neutralino decay to $Z\tilde{\chi}_1^0$, depending on the decay modes of W and Z bosons, can increase the jet multiplicity and missing transverse momentum.

This document presents two approaches to search for these sparticles in final states containing only hadronic jets and large missing transverse momentum. The first summarizes the most recent search results of the analysis [11] (referred to as 'Meff-based search' in the following). The second is the complementary search using the Recursive Jigsaw Reconstruction (RJR) techniques [12] in the construction of a discriminating variable set ('RJR-based search'). By using a dedicated set of selection criteria, the RJR-search improves the sensitivity to supersymmetric models with small mass splittings between the sparticles (models with compressed spectra). Both searches presented here adopt the same analysis strategy as the previous ATLAS search designed for the analysis of the 7 TeV, 8 TeV and 13 TeV data collected during Run 1 and Run 2 of the LHC, described in Refs. [11, 13–17]. The CMS Collaboration has set limits on similar models in Refs. [18–26].

In the searches presented here, events with reconstructed electrons or muons are rejected to reduce the background from events with neutrinos ($W \to e\nu, \mu\nu$) and to avoid any overlap with a complementary ATLAS search in final states with one lepton, jets and missing transverse momentum [27]. The selection criteria are optimized in the $(m_{\tilde{g}}, m_{\tilde{\chi}_1^0})$ and $(m_{\tilde{q}}, m_{\tilde{\chi}_1^0})$ planes, (where $m_{\tilde{g}}$, $m_{\tilde{q}}$ and $m_{\tilde{\chi}_1^0}$ are the gluino, squark and the LSP masses, respectively) for simplified models [28–30] in which all other supersymmetric particles are assigned masses beyond the reach of the LHC. Although interpreted in terms of SUSY models, the results of this analysis could also constrain any model of new physics that predicts the production of jets in association with missing transverse momentum.

The document is organized as follows. Section 2 describes the ATLAS experiment and the data sample used, and Section 3 the Monte Carlo (MC) simulation samples used for background and signal modelling. The physics object reconstruction and identification are presented in Section 4. A description of the recursive jigsaw technique and new variables is given in Section 5, and the analysis strategy used by both searches is given in Section 6. Searches are performed in signal regions which are defined in

Section 7. A summary of systematic uncertainties is presented in Section 9. Results obtained using the signal regions optimized for both searches are reported in Section 10. Section 11 is devoted to a summary and conclusions.

2. The ATLAS detector and data samples

The ATLAS detector [31] is a multi-purpose detector with a forward-backward symmetric cylindrical geometry and nearly 4π coverage in solid angle.[1] The inner tracking detector (ID) consists of pixel and silicon microstrip detectors covering the pseudorapidity region $|\eta| < 2.5$, surrounded by a transition radiation tracker which improves electron identification over the region $|\eta| < 2.0$. The innermost pixel layer, the insertable B-layer [32], was added between Run 1 and Run 2 of the LHC, at a radius of 33 mm around a new, narrower and thinner, beam pipe. The ID is surrounded by a thin superconducting solenoid providing an axial 2 T magnetic field and by a fine-granularity lead/liquid-argon (LAr) electromagnetic calorimeter covering $|\eta| < 3.2$. A steel/scintillator-tile calorimeter provides hadronic coverage in the central pseudorapidity range ($|\eta| < 1.7$). The endcap and forward regions ($1.5 < |\eta| < 4.9$) of the hadronic calorimeter are made of LAr active layers with either copper or tungsten as the absorber material. The muon spectrometer with an air-core toroid magnet system surrounds the calorimeters. Three layers of high-precision tracking chambers provide coverage in the range $|\eta| < 2.7$, while dedicated chambers allow triggering in the region $|\eta| < 2.4$.

The ATLAS trigger system [33, 34] consists of two levels; the first level is a hardware-based system, while the second is a software-based system called the High-Level Trigger. The events used by the searches presented in this document were selected using a trigger logic that accepts events with a missing transverse momentum above 70 GeV calculated using a sum over calorimeter cells (for data collected during 2015) or 100 GeV calculated using a scalar sum of the jet transverse momenta (for data collected in 2016). The trigger is 100% efficient for the event selections considered in these analyses. Auxiliary data samples used to estimate the yields of background events were selected using triggers requiring at least one isolated electron ($p_{\mathrm{T}} > 24$ GeV), muon ($p_{\mathrm{T}} > 20$ GeV) or photon ($p_{\mathrm{T}} > 120$ GeV) for data collected in 2015. For the 2016 data, the background events were selected using triggers requiring at least one isolated electron or muon ($p_{\mathrm{T}} > 26$ GeV) or photon ($p_{\mathrm{T}} > 140$ GeV).

The data were collected by the ATLAS detector during 2015 with a peak delivered instantaneous luminosity of $L = 5.2 \times 10^{33}$ cm^{-2}s^{-1}, and during 2016 with a corresponding peak delivered instantaneous luminosity of 1.1×10^{34} cm^{-2}s^{-1}, with a mean number of additional pp interactions per bunch crossing in the dataset of $\langle\mu\rangle = 14$ in 2015 and $\langle\mu\rangle = 21$ in 2016. Application of beam, detector and data-quality criteria resulted in a total integrated luminosity of 13.3 fb^{-1}. The uncertainty on the integrated luminosity is ±2.9%. It is derived, following a methodology similar to that detailed in Ref. [35], from a preliminary calibration of the luminosity scale using a pair of x–y beam-separation scans performed in August 2015 and June 2016.

[1] ATLAS uses a right-handed coordinate system with its origin at the nominal interaction point in the centre of the detector. The positive x-axis is defined by the direction from the interaction point to the centre of the LHC ring, with the positive y-axis pointing upwards, while the beam direction defines the z-axis. Cylindrical coordinates (r, ϕ) are used in the transverse plane, ϕ being the azimuthal angle around the z-axis. The pseudorapidity η is defined in terms of the polar angle θ by $\eta = -\ln\tan(\theta/2)$ and the rapidity is defined as $y = (1/2)\ln[(E + p_z)/(E - p_z)]$ where E is the energy and p_z the longitudinal momentum of the object of interest. The transverse momentum p_{T}, the transverse energy E_{T} and the missing transverse momentum $E_{\mathrm{T}}^{\mathrm{miss}}$ are defined in the x–y plane unless stated otherwise.

3. Monte Carlo simulated samples

A common set of simulated Monte Carlo (MC) data samples is used by both searches presented in this document to optimize the selections, estimate backgrounds and assess the sensitivity to specific SUSY signal models.

In this document SUSY signals are described by simplified models. They are defined by an effective Lagrangian describing the interactions of a small number of new particles, assuming one production process and one decay channel with a 100% branching fraction. Signal samples are used to describe squark- and gluino-pair production, followed by the direct decays of squarks ($\tilde{q} \to q\tilde{\chi}_1^0$) and direct ($\tilde{g} \to q\bar{q}\tilde{\chi}_1^0$) or one-step ($\tilde{g} \to q\bar{q}W\tilde{\chi}_1^0$, $\tilde{g} \to q\bar{q}Z\tilde{\chi}_1^0$) decays of gluinos as shown in Figure 1. Direct decays are those where the considered SUSY particles decay directly into SM particles and the LSP, while the one-step decays refer to the cases where the decays occur via one intermediate on-shell SUSY particle, as indicated in parentheses. These samples are generated with up to two extra partons in the matrix element using MG5_aMC@NLO 2.2.2 event generator [36] interfaced to Pythia 8.186 [37]. The CKKW-L merging scheme [38] is applied with a scale parameter that is set to a quarter of the mass of the gluino for $\tilde{g}\tilde{g}$ production or of the squark for $\tilde{q}\tilde{q}$ production. The A14 [39] set of tuned parameters (tune) is used for underlying event together with the NNPDF2.3LO [40] parton distribution function (PDF) set. The EvtGen v1.2.0 program [41] is used to describe the properties of the b- and c- hadron decays in the signal samples, and the background samples except those produced with Sherpa [42]. The signal cross-sections are calculated at next-to-leading order (NLO) in the strong coupling constant, adding the resummation of soft gluon emission at next-to-leading-logarithmic accuracy (NLO+NLL) [43–47]. The nominal cross-section is taken from an envelope of cross-section predictions using different PDF sets and factorization and renormalization scales, as described in Ref. [48], considering only light-flavour quarks (u, d, s, c). For the light-flavour squarks (gluinos) in case of gluino- (squark-) pair production, cross-sections are evaluated assuming masses of 450 TeV. The free parameters are $m_{\tilde{\chi}_1^0}$ and $m_{\tilde{q}}$ ($m_{\tilde{g}}$) for gluino-pair (squark-pair) production models.

The production of W or Z bosons in association with jets [49] is simulated using the Sherpa 2.2.0 generator, while the production of γ in association with jets is simulated using the Sherpa 2.1.1 generator. For W or Z bosons, the matrix elements are calculated for up to two partons at NLO and up to two additional partons at leading order (LO) using the Comix [50] and OpenLoops [51] matrix-element generators, and merged with the Sherpa parton shower [52] using the ME+PS@NLO prescription [53]. The samples are produced with a simplified scale setting prescription in the multi-parton matrix elements, to improve the event generation speed. A theory-based re-weighting of the jet multiplicity distribution is applied at event level, derived from event generation with the strict scale prescription. Events containing a photon in association with jets are generated requiring a photon transverse momentum above 35 GeV. For these events, matrix elements are calculated at LO with up to three or four partons depending on the p_{T} of the photon, and merged with the Sherpa parton shower using the ME+PS@LO prescription [54]. In the case of W/Z+jets, the NNPDF3.0NNLO PDF set [55] is used, while for the γ+jets production the CT10 PDF set [56] is used, both in conjunction with dedicated parton shower-tuning developed by the authors of Sherpa. The W/Z + jets events are normalized to their NNLO cross-sections [57]. For the γ+jets process the LO cross-section, taken directly from the Sherpa MC generator, is multiplied by a correction factor as described in Section 8.

For the generation of $t\bar{t}$ and single-top processes in the Wt and s-channel [58], the Powheg-Box v2 [59] generator is used with the CT10 PDF set. The electroweak (EW) t-channel single-top events are generated

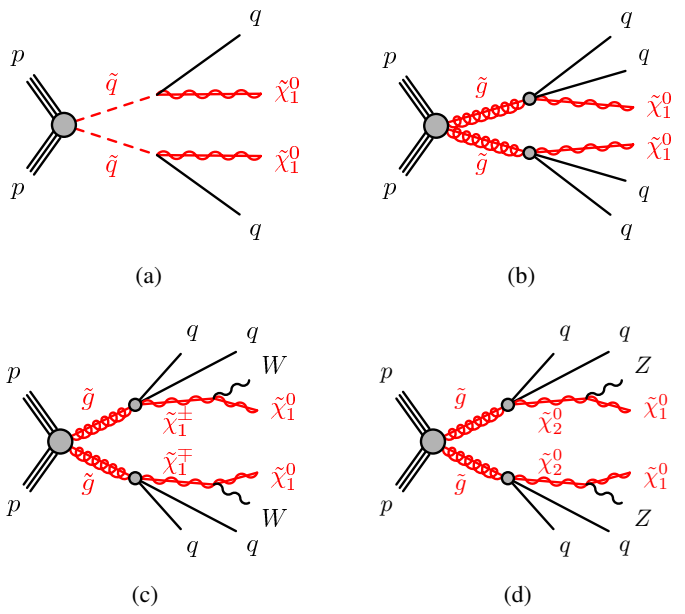

Figure 1: The decay topologies of (a) squark-pair production and (b, c, d) gluino-pair production, in the simplified models with (a) direct decays of squarks and (b) direct or (c, d) one-step decays of gluinos.

using the Powheg-Box v1 generator. This generator uses the four-flavour scheme for the NLO matrix-element calculations together with the fixed four-flavour PDF set CT10f4 [56]. For this process, the decay of the top quark is simulated using MadSpin tool [60] preserving all spin correlations, while for all processes the parton shower, fragmentation, and the underlying event are generated using Pythia 6.428 [61] with the CTEQ6L1 [62] PDF set and the corresponding Perugia 2012 tune (P2012) [63]. The top quark mass is set to 172.5 GeV. The h_{damp} parameter, which controls the p_{T} of the first additional emission beyond the Born configuration, is set to the mass of the top quark. The main effect of this is to regulate the high-p_{T} emission against which the ttbar system recoils [58]. The $t\bar{t}$ events are normalized to the NNLO+NNLL [64, 65]. The s- and t-channel single-top events are normalized to the NLO cross-sections [66, 67], and the Wt-channel single-top events are normalized to the NNLO+NNLL [68, 69].

For the generation of $t\bar{t}$ + EW processes ($t\bar{t}+W/Z/WW$) [70], the MG5_aMC@NLO 2.2.3 [36] generator at LO interfaced to the Pythia 8.186 parton-shower model is used, with up to two ($t\bar{t}+W$, $t\bar{t}+Z(\to \nu\nu/qq)$), one ($t\bar{t}+Z(\to \ell\ell)$) or no ($t\bar{t}+WW$) extra partons included in the matrix element. The ATLAS underlying-event tune A14 is used together with the NNPDF2.3LO PDF set. The events are normalized to their respective NLO cross-sections [71, 72].

Diboson processes (WW, WZ, ZZ) [73] are simulated using the Sherpa 2.1.1 generator. For processes with four charged leptons (4ℓ), three charged leptons and a neutrino (3ℓ+1ν) or two charged leptons and two neutrinos (2ℓ+2ν), the matrix elements contain all diagrams with four electroweak vertices, and are calculated for up to one (4ℓ, 2ℓ+2ν) or no partons (3ℓ+1ν) at NLO and up to three partons at LO using the Comix and OpenLoops matrix-element generators, and merged with the Sherpa parton shower using the ME+PS@NLO prescription. For processes in which one of the bosons decays hadronically and the other leptonically, matrix elements are calculated for up to one (ZZ) or no (WW, WZ) additional partons at NLO and for up to three additional partons at LO using the Comix and OpenLoops matrix-element generators,

and merged with the SHERPA parton shower using the ME+PS@NLO prescription. In all cases, the CT10 PDF set is used in conjunction with a dedicated parton-shower tuning developed by the authors of SHERPA. The generator cross-sections are used in this case.

The multi-jet background is generated with PYTHIA 8.186 using the A14 underlying-event tune and the NNPDF2.3LO parton distribution functions.

A summary of the SM background processes together with the MC generators, cross-section calculation orders in α_s, PDFs, parton shower and tunes used is given in Table 1.

Physics process	Generator	Cross-section normalization	PDF set	Parton shower	Tune
$W(\rightarrow \ell\nu)$ + jets	SHERPA 2.2.0	NNLO	NNPDF3.0NNLO	SHERPA	SHERPA default
$Z/\gamma^*(\rightarrow \ell\bar{\ell})$ + jets	SHERPA 2.2.0	NNLO	NNPDF3.0NNLO	SHERPA	SHERPA default
γ + jets	SHERPA 2.1.1	LO	CT10	SHERPA	SHERPA default
$t\bar{t}$	POWHEG-BOX v2	NNLO+NNLL	CT10	PYTHIA 6.428	PERUGIA2012
Single top (Wt-channel)	POWHEG-BOX v2	NNLO+NNLL	CT10	PYTHIA 6.428	PERUGIA2012
Single top (s-channel)	POWHEG-BOX v2	NLO	CT10	PYTHIA 6.428	PERUGIA2012
Single top (t-channel)	POWHEG-BOX v1	NLO	CT10f4	PYTHIA 6.428	PERUGIA2012
$t\bar{t}+W/Z/WW$	MG5_aMC@NLO 2.2.3	NLO	NNPDF2.3LO	PYTHIA 8.186	A14
WW, WZ, ZZ	SHERPA 2.1.1	NLO	CT10	SHERPA	SHERPA default
Multi-jet	PYTHIA 8.186	LO	NNPDF2.3LO	PYTHIA 8.186	A14

Table 1: The Standard Model background Monte Carlo simulation samples used in this paper. The generators, the order in α_s of cross-section calculations used for yield normalization, PDF sets, parton showers and tunes used for the underlying event are shown.

For all SM background samples the response of the detector to particles is modelled with a full ATLAS detector simulation [74] based on GEANT4 [75]. Signal samples are prepared using a fast simulation based on a parameterization of the performance of the ATLAS electromagnetic and hadronic calorimeters [76] and on GEANT4 elsewhere.

All simulated events are overlaid with multiple pp collisions simulated with the soft QCD processes of PYTHIA 8.186 using the A2 tune [39] and the MSTW2008LO parton distribution functions [77]. The simulations are reweighted to match the distribution of the mean number of interactions observed in data.

4. Object reconstruction and identification

The reconstructed primary vertex of the event is required to be consistent with the luminous region and to have at least two associated tracks with $p_T > 400$ MeV. When more than one such vertex is found, the vertex with the largest $\sum p_T^2$ of the associated tracks is chosen.

Jet candidates are reconstructed using the anti-k_t jet clustering algorithm [78, 79] with jet radius parameter of 0.4 and starting from clusters of calorimeter cells [80]. The jets are corrected for energy from pile-up using the method described in Ref. [81]: a contribution equal to the product of the jet area and the median energy density of the event is subtracted from the jet energy [82]. Further corrections, referred to as the jet energy scale corrections, are derived from MC simulation and data and used to calibrate on average the energies of jets to the scale of their constituent particles [83]. Only jet candidates with $p_T > 20$ GeV and $|\eta| < 2.8$ after all corrections are retained. An algorithm based on boosted decision trees, 'MV2c10'

[84, 85], is used to identify jets containing a b-hadron (b-jets), with an operating point corresponding to an efficiency of 77%, along with the rejection factors of 134 for light-quark jets and 6 for charm jets [85]. Candidate b-tagged jets are required to have $p_{\mathrm{T}} > 50$ GeV and $|\eta| < 2.5$. Events with jets originating from detector noise and non-collision background are rejected if the jets fail to satisfy the 'LooseBad' quality criteria, or if at least one of the two leading jets with $p_{\mathrm{T}} > 100$ GeV fails to satisfy the 'TightBad' quality criteria, both described in Ref. [86]. These selections affect less than 1% of the events used in the search. In order to reduce the number of jets coming from pile-up, a significant fraction of the tracks associated with each jet must have an origin compatible with the primary vertex, as defined by the jet vertex tagger (JVT) output [87]. The requirement JVT > 0.59 is only applied to jets with $p_{\mathrm{T}} < 60$ GeV and $|\eta| < 2.4$.

Two different classes of reconstructed lepton candidates (electrons or muons) are used in the analyses presented here. When selecting samples used for the search, events containing a 'baseline' electron or muon are rejected. The selections applied to identify baseline leptons are designed to maximize the efficiency with which W+jets and top quark background events are rejected. When selecting 'control region' samples for the purpose of estimating residual W+jets and top quark backgrounds, additional requirements are applied to leptons to ensure greater purity of these backgrounds. These leptons are referred to as 'high-purity' leptons below and form a subset of the baseline leptons.

Baseline muon candidates are formed by combining information from the muon spectrometer and inner tracking detectors as described in Ref. [88] and are required to have $p_{\mathrm{T}} > 10$ GeV and $|\eta| < 2.7$. High-purity muon candidates must additionally have $|\eta| < 2.4$, the significance of the transverse impact parameter with respect to the primary vertex, $|d_0^{\mathrm{PV}}|/\sigma(d_0^{\mathrm{PV}}) < 3$, the longitudinal impact parameter with respect to the primary vertex $|z_0^{\mathrm{PV}}\sin(\theta)| < 0.5$ mm, and to satisfy 'GradientLoose' isolation requirements described in Ref. [88] which rely on the use of tracking-based and calorimeter-based variables and implement a set of η- and p_{T}-dependent criteria. The leading, high-purity muon, is also required to have $p_{\mathrm{T}} > 27$ GeV.

Baseline electron candidates are reconstructed from an isolated electromagnetic calorimeter energy deposit matched to an ID track and are required to have $p_{\mathrm{T}} > 10$ GeV, $|\eta| < 2.47$, and to satisfy 'Loose' likelihood-based identification criteria described in Ref. [89]. High-purity electron candidates additionally must satisfy 'Tight' selection criteria described in Ref. [89], and the leading electron must have $p_{\mathrm{T}} > 27$ GeV. They are also required to have $|d_0^{\mathrm{PV}}|/\sigma(d_0^{\mathrm{PV}}) < 5$, $|z_0^{\mathrm{PV}}\sin(\theta)| < 0.5$ mm, and to satisfy similar isolation requirements as those applied to high-purity muons.

After the selections described above, ambiguities between candidate jets with $|\eta| < 2.8$ and leptons are resolved as follows: first, any such jet candidate which is not tagged as b-jet, lying within a distance $\Delta R \equiv \sqrt{(\Delta y)^2 + (\Delta\phi)^2} = 0.2$ of a baseline electron is discarded. If a jet candidate is b-tagged, the object is interpreted as a jet and the overlapping electron is ignored. Additionally, if a baseline electron (muon) and a jet passing the JVT selection described above are found within $0.2 \leq \Delta R < 0.4$ ($\Delta R <$min(0.4, 0.04 + 10 GeV/p_{T}^{μ})), the object is interpreted as a jet and the nearby electron (muon) candidate is discarded. Finally, if a baseline muon and jet are found within $\Delta R < 0.2$, the object is treated as a muon and the overlapping jet is ignored if the jet satisfies the following criteria: $N_{\mathrm{trk}} < 3$ or $\left(p_{\mathrm{T}}^{\mu} > 0.7 \sum p_{\mathrm{T}}^{\mathrm{trk}} \text{ and } p_{\mathrm{T}}^{\mathrm{jet}} < 0.5 p_{\mathrm{T}}^{\mu}\right)$, where N_{trk} refers to the number of tracks with $p_{\mathrm{T}} > 500$ MeV that are to the jet, and $\sum p_{\mathrm{T}}^{\mathrm{trk}}$ is the sum of their transverse momenta. These criteria are intended to identify jets consistent with final state radiation or hard bremsstrahlung.

Additional ambiguities between electrons and muons in a jet, originating from the decays of hadrons, are resolved to avoid double counting and/or remove non-isolated leptons: the electron is discarded if a baseline electron and a baseline muon share the same ID track.

The measurement of the missing transverse momentum vector $\boldsymbol{E}_{\mathrm{T}}^{\mathrm{miss}}$ (and its magnitude $E_{\mathrm{T}}^{\mathrm{miss}}$) is based on the calibrated transverse momenta of all electron, muon, photon and jet candidates and all tracks originating from the primary vertex and not associated with such objects [90].

Reconstructed photons are not used in the main signal-event selection, but are used to select in the region to constrain the Z+jets background, as explained in Section 8. Photon candidates are required to satisfy $p_{\mathrm{T}} > 150$ GeV and $|\eta| < 2.37$, photon shower shape and electron rejection criteria [91], and to be isolated. Ambiguities between candidate jets and photons (when used in the event selection) are resolved by discarding any jet candidates lying within $\Delta R = 0.4$ of a photon candidate. Additional selections to remove ambiguities between electrons or muons and photons are applied such that the photon is discarded if it is within $\Delta R = 0.4$ of an electron or muon.

Corrections derived from data control samples are applied to account for differences between data and simulation for the lepton trigger and reconstruction efficiencies, the lepton momentum/energy scale and resolution, and for the efficiency and mis-tag rate of the b-tagging algorithm.

5. The Recursive Jigsaw Reconstruction technique

The Recusive Jigsaw Reconstruction technique is a method used as a basis for defining the kinematic variables on an event-by-event level. While it is straightforward to fully describe an event's underlying kinematic features when all objects are fully reconstructed, events involving weakly interacting particles present a challenge, as the loss of information constrains the kinematic variable construction to take place in the lab frame instead of the more physically natural frames of the hypothesized decays. The deconstruction of the available kinematic information into factorizable information is only possible given a set of external constraints on the invisible system (e.g. longitudinal boost invariance) and minimizations of the masses of intermediate particle states with respect to unknown quantities.

Given a rule for applying additional information to the invisible system, known here as a *jigsaw*, a specific underlying decay hypothesis can be imposed on the event. The RJR algorithm is an inter-changeable rule for resolving a kinematic or combinatoric ambiguities. By viewing the event in a certain decay topology and accounting for the assumptions for the lost degrees of freedom, a four-momentum hypothesis is assigned to each invisible state. Once all four-momenta are defined, the RJR variable construction involves boosting into proxy rest frames for each intermediate hypothesized particle. In these rest frames, kinematic variables can be computed, and for the correct decay tree topology, variables from different rest frames should encode different information and be therefore uncorrelated. A natural basis of observables is then the one associated with this decay tree. The available variables can depend on the decay tree topology used.

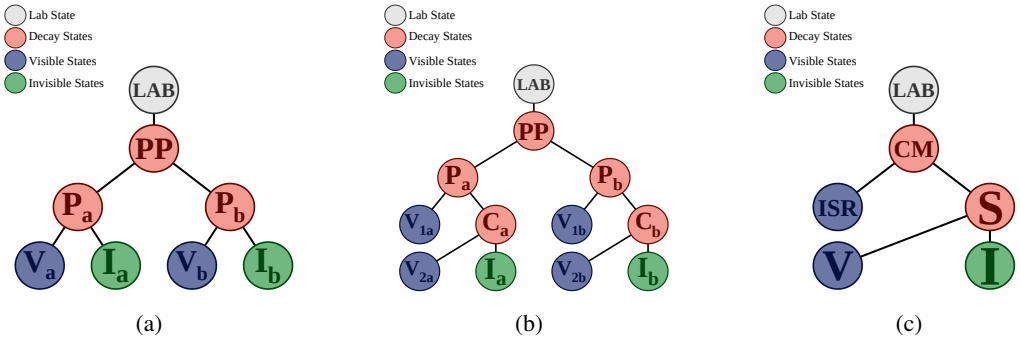

Figure 2: (a) Inclusive strong sparticle production decay tree. Two sparticles (P_a and P_b) are non-resonantly pair-produced with each decaying to one or more visible particles (V_a and V_b) which are reconstructed in the detector, and two systems of invisble particles (I_a and I_b) whose four-momenta are only partially constrained. (b) An additional level of decays can be added to the left tree when requiring more than two visible objects. This tree is particularly useful for the search for gluino pair-production described in the text. (c) Strong sparticle production with ISR decay tree for use with small mass-splitting spectra. A signal sparticle system S decaying to a set of visible momenta V and invisible momentum I recoils off of a jet radiation system ISR.

In searches for strong production of sparticles in R-parity conserving models, one can impose the decay tree shown in Figure 2(a). Each event is analyzed as if two sparticles (the intermediate states P_a and P_b) were produced and then decayed to the particles observed in our detector (the collections V_a and V_b). The benchmark signal models probed in this search give rise to signal events with at least two weakly-interacting particles associated with two systems of particles (I_a and I_b), the respective children of the initially produced sparticles.

This decay tree includes several kinematic and combinatoric unknowns. In the final state with no leptons, the objects observed in the detector are exclusively jets and one must decide how to partition these jets into the two groups V_a and V_b in order to calculate the observables associated with the decay tree. In this case, the grouping that minimizes the masses of the four-vector sum of group constituents is chosen.

More explicitly, the collection of reconstructed jet four-vectors, $V \equiv \{p_i\}$ and their four-vector sum p_V are considered. Each of the four-momenta is evaluated in the rest-frame of p_V (V-frame) and different partitionings of these jets $V_i = \{p_1, \cdots, p_{N_i}\}$ are considered such that $V_a \bigcap V_b = 0$ and $V_a \bigcup V_b = V$. For each partition, the sum of four-vectors $p_{V_i}^V = \sum_j^{N_i} p_j^V$ is calculated and the combination chosen that maximizes the momenta of the two groups, $|\vec{p}_{V_a}^V| + |\vec{p}_{V_b}^V|$. The axis that this partition implicitly defines in the V rest-frame is equivalent to the thrust-axis of the jets, and the masses $M_{V_i} = \sqrt{p_{V_i}^2}$ have, in a sense, been simultaneously minimized. When analyzing the entire event, these two groups are called "jet hemispheres."

The remaining unknowns in the event are associated with the two collections of weakly interacting particles: their masses, longitudinal momenta and information as how the two groups independently contribute to the $\boldsymbol{E}_T^{miss}$. The RJR algorithm organizes these unknowns into the groups of necessary information for determining the relative velocities of the reference frames in the decay tree, or the boosts that relate them to each other. The algorithm then proceeds from the first known reference frame, the lab frame, and traverses the decay tree through each intermediate frame. When unknowns are encountered

that are necessary to determine the following boosts, a jigsaw rule of choosing always the mass minimization of the hemispheres is applied to resolve the necessary information.

In each of these newly constructed rest frames, all relevant momenta are defined and can be used to construct any variable – multi-object invariant masses, angles between objects, etc. The primary scale-sensitive variables used in the search presented here are a suite of scale variables denoted by H. These H variables derive their name from H_{T}, the scalar sum of visible transverse momenta. However, in contrast to H_{T}, these H variables are constructed with aggregate momenta, including contributions from the invisible four-momenta, and are not necessarily evaluated in the lab frame, nor only in the transverse plane.

The H variables are labeled with a superscript F and two subscripts n and m, $H^{F}_{\mathrm{n,m}}$. The F represents the rest frame in which the momenta are evaluated. In this analysis, this may be the lab frame, the proxy frame for the sparticle-sparticle frame PP, or the proxy frame for an individual sparticle's rest frame P. The subscripts n and m represent the number of visible and invisible momentum vectors considered, respectively. This means given the number of visible momentum vectors in the frame, these will be summed together until there remain only n distinct vectors. The choice for which vectors are summed is made by finding jets nearest in phase space. This is done using the same mass-minimization procedure used in the frame construction. This procedure tends to join, for example, a hard jet with a soft near-by radiated jet. The same is done for the invisible system into m vectors. For events with fewer than n visible objects the sum will only run over the available vectors. The additional subscript T can denote a transverse version of the variable where the transverse plane is defined with respect to the velocity of the frame F. In practice, this is similar to the plane transverse to the beam-line. The purposeful obfuscation of information into aggregate momenta allows for the same event to be interpreted in several independent ways such that each H variable encodes unique information.

In addition to scale-sensitive variables, the power of the RJR technique comes from the ensemble of variables that can be constructed and used in concert with the H variables with minimal correlation. It is therefore useful to categorize variables into those sensitive to scale (generally having units of GeV) and those that are unitless and scale-invariant. In the limit that one only places requirements on scale-invariant variables, there is no dependence on the sparticle spectrum and the sensitivity to compressed spectra is improved. In practice, this can guide the construction of regions targeting compressed spectra where stricter requirements on scale-invariant variables can be emphasized.

Given the plethora of choices the RJR technique provides, the variables that are used to define the signal and control regions, described in the document are listed below. The paradigm of the RJR analysis design is to use as few requirements with units GeV as possible. The sensitivity of the analysis is amplified by marrying a minimal set of scale variables requirements with selections imposed on unitless quantities.

To select signal events in models with squark-pair production, the following variables are used:

- $H^{\mathrm{PP}}_{1,1}$ → scale variable as described above. Similar to $E^{\mathrm{miss}}_{\mathrm{T}}$.
- $H^{\mathrm{PP}}_{\mathrm{T}\,2,1}$ → scale variable as described above. Similar to effective mass, m_{eff} (defined as the scalar sum of the transverse momenta of the leading two jets and $E^{\mathrm{miss}}_{\mathrm{T}}$) for squark-pair production signals with two-jet final states.
- $H^{\mathrm{PP}}_{1,1}/H^{\mathrm{PP}}_{2,1}$ → provides additional information in testing the balance of the information provided by the two scale cuts, where in the denominator the $H^{\mathrm{PP}}_{2,1}$ is no longer solely transverse. This provides

an excellent handle against imbalanced events where the large scale is dominated by a particular object p_{T} or by high $E_{\mathrm{T}}^{\mathrm{miss}}$.

- $p_{\mathrm{z}}^{\mathrm{lab}}/(p_{\mathrm{z}}^{\mathrm{lab}} + H_{\mathrm{T}\ 2,1}^{\mathrm{PP}}) \rightarrow$ compares the z-momentum of the lab frame to the overall transverse scale variable considered. This variable tests for significant boost in the z direction.
- $p_{\mathrm{Tj2}}^{\mathrm{PP}}/H_{\mathrm{T}\ 2,1}^{\mathrm{PP}} \rightarrow$ represents the fraction of the overall scale variable that is due to the second highest p_{T} jet (in the PP frame) in the event.

For signal topologies with higher jet multiplicities, there is the option to exploit the internal structure of the hemispheres by using a decay tree with an additional decay. For gluino-pair production, the tree shown in Figure 2(b) can be used and the variables used by this search are:

- $H_{1,1}^{\mathrm{PP}} \rightarrow$ described above.
- $H_{\mathrm{T}\ 4,1}^{\mathrm{PP}} \rightarrow$ analogous to the transverse scale variable described above but more appropriate for four-jet final states expected from gluino-pair production.
- $H_{1,1}^{\mathrm{PP}}/H_{4,1}^{\mathrm{PP}} \rightarrow$ analogous to $H_{1,1}^{\mathrm{PP}}/H_{2,1}^{\mathrm{PP}}$ for the squark search.
- $H_{\mathrm{T}\ 4,1}^{\mathrm{PP}}/H_{4,1}^{\mathrm{PP}} \rightarrow$ a measure of the fraction of the momentum that lies in the transverse plane.
- $p_{\mathrm{z}}^{\mathrm{lab}}/(p_{\mathrm{z}}^{\mathrm{lab}} + H_{\mathrm{T}\ 4,1}^{\mathrm{PP}}) \rightarrow$ analogous to $p_{\mathrm{z}}^{\mathrm{lab}}/(p_{\mathrm{z}}^{\mathrm{lab}} + H_{\mathrm{T}\ 2,1}^{\mathrm{PP}})$ above.
- min $(p_{\mathrm{Tj2i}}^{\mathrm{PP}}/H_{\mathrm{T}\ 2,1\mathrm{i}}^{\mathrm{PP}}) \rightarrow$ represents the fraction of a hemisphere's overall scale due to the second highest p_{T} jet (in the PP frame) in each hemisphere. The minimum value between the two hemispheres is used.
- max $(H_{1,0}^{\mathrm{P_i}}/H_{2,0}^{\mathrm{P_i}}) \rightarrow$ testing balance of solely the jets momentum in a given hemisphere allows an additional handle against a small but pernicious subset of events.
- $|\frac{2}{3}\Delta\phi_{\mathrm{V,P}}^{\mathrm{PP}} - \frac{1}{3}\cos\theta_{\mathrm{P}}| \rightarrow$ constructed from the difference between the azimuthal angle between the V and P frames, evaluated in the PP frame and the polar angle of that parent particle. The difference between these two angular properties highlights events where the missing transverse momentum is imbalanced between hemispheres (e.g. semileptonic $t\bar{t}$ decays where the lepton is reconstructed as a jet). This variable exploits the fact that signal events tend to be more "spherical" to efficiently suppress these pernicious background sources.

In addition to trying to resolve the entirety of the signal event, it can be useful for sparticle spectra with smaller mass splittings and lower intrinsic $E_{\mathrm{T}}^{\mathrm{miss}}$ to instead select for a partially-resolved sparticle system recoiling off of a high-p_{T} jet from initial state radiation (ISR). To target such topologies, a separate tree targeting compressed spectra can be seen in Figure 2(c). This tree is somewhat simpler and attempts to identify visible (V) and invisible (I) systems that are the result of an intermediate state S. This signal system is required to recoil off of a system of visible momenta associated with the ISR. This tree yields a slightly different set of variables:

- $|p_{\mathrm{TS}}^{\mathrm{ISR}}| \rightarrow$ the magnitude of the vector-summed transverse momenta of all ISR-associated jets evaluated in the CM frame.

- $R_{\mathrm{ISR}} \equiv \vec{p}_{\mathrm{I}}^{\,\mathrm{CM}} \cdot \hat{p}_{\mathrm{TS}}^{\,\mathrm{CM}} / p_{\mathrm{TS}}^{\mathrm{CM}} \rightarrow$ serves as a proxy for $m_{\tilde{\chi}}/m_{\tilde{\mathrm{p}}}$. $\rightarrow$ This is the fraction of the boost of the S system that is carried by its invisible system I. As the $|p_{\mathrm{TS}}^{\mathrm{ISR}}|$ is increased it becomes increasingly hard for backgrounds to possess a large value in this ratio - a feature exhibited by compressed signals.
- $M_{\mathrm{TS}} \rightarrow$ the transverse mass of the S system.
- $N_{\mathrm{jet}}^{\mathrm{V}} \rightarrow$ number of jets assigned to the visible system (V) and not associated with the ISR system.
- $\Delta\phi_{\mathrm{ISR,I}} \rightarrow$ This is the opening angle between the ISR system and the invisible system in the lab frame.

6. Analysis strategy and fit description

This section summarizes the common analysis strategy and statistical techniques that are employed in the searches presented in this document.

To search for a possible signal, selections are defined to enhance the signal relative to the SM background. Signal regions (SRs) are defined using the Monte Carlo simulation of the signal processes and the SM backgrounds. They are optimized to maximize the expected significance for each model considered. To estimate the SM backgrounds in a consistent and robust fashion, corresponding control regions (CRs) are defined for each of the signal regions. They are chosen to be non-overlapping with the SR selections in order to provide independent data samples enriched in particular background sources, and are used to normalize the background MC simulation. The CR selections are optimized to have negligible SUSY signal contamination for the models near the previously excluded boundary [16], while minimizing the systematic uncertainties arising from the extrapolation of the CR event yields to estimate backgrounds in the SR. Cross-checks of the background estimates are performed with data in several validation regions (VRs) selected with requirements such that these regions do not overlap with the CR and SR selections, and also have a low expected signal contamination.

To extract the final results, three different classes of likelihood fit are employed: background-only, model-independent and model-dependent fits [92]. A background-only fit is used to estimate the background yields in each SR. The fit is performed using the observed event yields from the CRs associated with the SR as the only constraints, and not the SR itself. It is assumed that signal events from physics beyond the Standard Model (BSM) do not contribute to these yields. The scale factors ($\mu_{W+\mathrm{jets}}, \mu_{Z+\mathrm{jets}}, \mu_{\mathrm{Top}}, \mu_{\mathrm{Multi-jet}}$) are fitted in each CR attached to a SR. The expected background in the SR is based on the yields predicted by simulation for W/Z+jets, top quark backgrounds, corrected by the scale factors derived from the fit. In case of multi-jet background, the estimate is based on the data-driven method described in Section 8. The systematic uncertainties and the MC statistical uncertainties in the expected values are included in the fit as nuisance parameters which are constrained by Gaussian distributions with widths corresponding to the sizes of the uncertainties considered and by Poisson distributions, respectively. The background-only fit is also used to estimate the background event yields in the VRs.

If no excess is observed, a model-independent fit is used to set upper limits on the number of BSM signal events in each SR. This fit proceeds in the same way as the background-only fit, except that the number of events observed in the SR is added as an input to the fit, and the BSM signal strength, constrained to be non-negative, is added as a free parameter. The observed and expected upper limits at 95% confidence level (CL) on the number of events from BSM phenomena for each signal region (S_{obs}^{95} and S_{exp}^{95}) are

derived using the CL_s prescription [93], neglecting any possible signal contamination in the control regions. These limits, when normalized by the integrated luminosity of the data sample, may be interpreted as upper limits on the visible cross-section of BSM physics ($\langle\epsilon\sigma\rangle^{95}_{\text{obs}}$), where the visible cross-section is defined as the product of production cross-section, acceptance and efficiency. The model-independent fit is also used to compute the one-sided p-value (p_0) of the background-only hypothesis, which quantifies the statistical significance of an excess.

Finally, model-dependent fits are used to set exclusion limits on the signal cross-sections for specific SUSY models. Such a fit proceeds in the same way as the model-independent fit, except that both the yield in the signal region and the signal contamination in the CRs are taken into account. Correlations between signal and background systematic uncertainties are taken into account where appropriate. Signal-yield systematic uncertainties due to detector effects and the theoretical uncertainties in the signal acceptance are included in the fit.

7. Event selection and signal regions definitions

Following the object reconstruction described in Section 4, in both searches documented here events are discarded if a baseline electron or muon with $p_{\text{T}} > 10$ GeV remains, or if they contain a jet failing to satisfy quality selection criteria designed to suppress detector noise and non-collision backgrounds (described in Section 4). Only events with a reconstructed primary vertex associated with two or more tracks are used further in the analyses. Events are rejected if no jets with $p_{\text{T}} > 50$ GeV are found. The remaining events are then analysed in two complementary searches, both of which require the presence of jets and significant missing transverse momentum. The selections in the two searches are designed to be generic enough to ensure sensitivity in a broad set of models with jets and $E_{\text{T}}^{\text{miss}}$ in the final state.

In order to maximize the sensitivity in the $(m_{\tilde{\text{g}}}, m_{\tilde{\text{q}}})$ plane, a variety of signal regions are defined. They are chosen by optimizing the value of the signal discovery significance for a signal mass hypothesis defined to provide the value close to a 3 σ significance. Squarks typically generate at least one jet in their decays, for instance through $\tilde{q} \rightarrow q\tilde{\chi}^0_1$, while gluinos typically generate at least two jets, for instance through $\tilde{g} \rightarrow q\bar{q}\tilde{\chi}^0_1$. Processes contributing to $\tilde{q}\tilde{q}$ and $\tilde{g}\tilde{g}$ final states therefore lead to events containing at least two or four jets, respectively. Decays of heavy SUSY and SM particles produced in longer $\tilde{q}$ and $\tilde{g}$ decay cascades (e.g. $\tilde{\chi}^{\pm}_1 \rightarrow qq'\tilde{\chi}^0_1$) tend to further increase the jet multiplicity in the final state. To target different scenarios, signal regions with different jet multiplicity requirements (in the case of Meff-based search) or different decay trees (in the case of RJR-based search) are assumed. Summary of optimized signal regions used by both searches are presented in the following.

7.1. The jets+$E_{\text{T}}^{\text{miss}}$ Meff-based search

Due to the high mass scale expected for the SUSY models considered in this study, the 'effective mass', m_{eff}, is a powerful discriminant between the signal and SM backgrounds. When selecting events with at least N_{j} jets, $m_{\text{eff}}(N_{\text{j}})$ is defined to be the scalar sum of the transverse momenta of the leading N_{j} jets and $E_{\text{T}}^{\text{miss}}$. Requirements placed on m_{eff} and $E_{\text{T}}^{\text{miss}}$ form the basis of the Meff-based search by strongly suppressing the multi-jet background where jet energy mismeasurement generates missing transverse momentum. The final signal selection uses requirements on both m_{eff}(incl.), which sums over all jets with $p_{\text{T}} > 50$ GeV and $E_{\text{T}}^{\text{miss}}$, which is required to be larger than 250 GeV.

Thirteen inclusive SRs characterized by increasing minimum jet multiplicity from two to six, are defined in Table 2: five regions targeting models characterized by the squark-pair production with the direct decay of squarks, six regions targeting models with gluino-pair production followed by the direct decay of gluinos and two regions targeting gluino-pair production followed by the one-step decay of gluino via an intermediate chargino. Signal regions requiring the same jet-multiplicity are distinguished by increasing the threshold of the m_{eff}(incl.) and $E_{\text{T}}^{\text{miss}}/m_{\text{eff}}(N_{\text{j}})$ (or $E_{\text{T}}^{\text{miss}}/\sqrt{H_{\text{T}}}$) requirements. This ensures the sensitivity to different mass differences for each decay mode. All signal regions corresponding to the Meff-based search have 'Meff' prefix.

In each region, different thresholds are applied on jet momenta and on $\Delta\phi(\text{jet}, \boldsymbol{E}_{\text{T}}^{\text{miss}})_{\text{min}}$, which is defined to be the smallest azimuthal separation between $\boldsymbol{E}_{\text{T}}^{\text{miss}}$ and the momenta of any of the reconstructed jets with $p_{\text{T}} > 50$ GeV. Requirements on $\Delta\phi(\text{jet}, \boldsymbol{E}_{\text{T}}^{\text{miss}})_{\text{min}}$ and $E_{\text{T}}^{\text{miss}}/m_{\text{eff}}(N_{\text{j}})$ are designed to reduce the background from multi-jet processes. For the 2-jet SRs which are optimized for squark-pair production followed by the direct decay of squarks, the selection requires $\Delta\phi(\text{jet}_{1,2,(3)}, \boldsymbol{E}_{\text{T}}^{\text{miss}})_{\text{min}} > 0.8$ using up to three leading (if jets present in the event), while in SRs with higher jet multiplicities the requirement $\Delta\phi(\text{jet}_{1,2,(3)}, \boldsymbol{E}_{\text{T}}^{\text{miss}})_{\text{min}} > 0.4$ is used. For the SRs requiring at least four, five or six jets in the final state, or in the case when more than three jets are present in 2-jet or 3-jet SRs, an additional requirement on $\Delta\phi(\text{jet}_{\text{i}>3}, \boldsymbol{E}_{\text{T}}^{\text{miss}})_{\text{min}}$ is applied to all jets.

In the 2-jet and 3-jet SRs the requirement on $E_{\text{T}}^{\text{miss}}/m_{\text{eff}}(N_{\text{j}})$ is replaced by a requirement on $E_{\text{T}}^{\text{miss}}/\sqrt{H_{\text{T}}}$ (where H_{T} is defined as the scalar sum of the transverse momenta of all jets), which is found to lead to enhanced sensitivity to models characterized by $\tilde{q}\tilde{q}$ production. In the other regions with at least four jets in the final state, additional suppression of background processes is based on the aplanarity variable, which is defined as $A = 3/2\lambda_3$, where λ_3 is the smallest eigenvalue of the normalized momentum tensor of the jets [94].

Targeted signal	$\tilde{q}\tilde{q}, \tilde{q} \rightarrow q\tilde{\chi}_1^0$				
Requirement	Signal Region				
	Meff-2j-800	**Meff-2j-1200**	**Meff-2j-1600**	**Meff-2j-2000**	**Meff-3j-1200**
$E_{\mathrm{T}}^{\mathrm{miss}}$ [GeV] >	250				
$p_{\mathrm{T}}(j_1)$ [GeV] >	200	250			600
$p_{\mathrm{T}}(j_2)$ [GeV] >	200	250			50
$p_{\mathrm{T}}(j_3)$ [GeV] >	–				50
$\lvert\eta(j_{1,2})\rvert$ <	0.8	1.2			–
$\Delta\phi(\mathrm{jet}_{1,2,(3)}, \boldsymbol{E}_{\mathrm{T}}^{\mathrm{miss}})_{\mathrm{min}}$ >	0.8				0.4
$\Delta\phi(\mathrm{jet}_{\mathrm{i}>3}, \boldsymbol{E}_{\mathrm{T}}^{\mathrm{miss}})_{\mathrm{min}}$ >	0.4				0.2
$E_{\mathrm{T}}^{\mathrm{miss}}/\sqrt{H_{\mathrm{T}}}$ [GeV$^{1/2}$] >	14	16	18	20	16
m_{eff}(incl.) [GeV] >	800	1200	1600	2000	1200

Targeted signal	$\tilde{g}\tilde{g}, \tilde{g} \rightarrow q\bar{q}\tilde{\chi}_1^0$					
Requirement	Signal Region					
	Meff-4j-1000	**Meff-4j-1400**	**Meff-4j-1800**	**Meff-4j-2200**	**Meff-4j-2600**	**Meff-5j-1400**
$E_{\mathrm{T}}^{\mathrm{miss}}$ [GeV] >	250					
$p_{\mathrm{T}}(j_1)$ [GeV] >	200					500
$p_{\mathrm{T}}(j_4)$ [GeV] >	100			150		50
$p_{\mathrm{T}}(j_5)$ [GeV] >	–					50
$\lvert\eta(j_{1,2,3,4})\rvert$ <	1.2	2.0			–	
$\Delta\phi(\mathrm{jet}_{1,2,(3)}, \boldsymbol{E}_{\mathrm{T}}^{\mathrm{miss}})_{\mathrm{min}}$ >	0.4					
$\Delta\phi(\mathrm{jet}_{\mathrm{i}>3}, \boldsymbol{E}_{\mathrm{T}}^{\mathrm{miss}})_{\mathrm{min}}$ >	0.4					0.2
Aplanarity >	0.04					–
$E_{\mathrm{T}}^{\mathrm{miss}}/m_{\mathrm{eff}}(N_{\mathrm{j}})$ >	0.25		0.2			0.3
m_{eff}(incl.) [GeV] >	1000	1400	1800	2200	2600	1400

Targeted signal	$\tilde{g}\tilde{g}, \tilde{g} \rightarrow q\bar{q}W\tilde{\chi}_1^0$	
Requirement	Signal Region	
	Meff-6j-1800	**Meff-6j-2200**
$E_{\mathrm{T}}^{\mathrm{miss}}$ [GeV] >	250	
$p_{\mathrm{T}}(j_1)$ [GeV] >	200	
$p_{\mathrm{T}}(j_6)$ [GeV] >	50	100
$\lvert\eta(j_{1,\ldots,6})\rvert$ <	2.0	–
$\Delta\phi(\mathrm{jet}_{1,2,(3)}, \boldsymbol{E}_{\mathrm{T}}^{\mathrm{miss}})_{\mathrm{min}}$ >	0.4	
$\Delta\phi(\mathrm{jet}_{\mathrm{i}>3}, \boldsymbol{E}_{\mathrm{T}}^{\mathrm{miss}})_{\mathrm{min}}$ >	0.2	
Aplanarity >	0.08	
$E_{\mathrm{T}}^{\mathrm{miss}}/m_{\mathrm{eff}}(N_{\mathrm{j}})$ >	0.2	0.15
m_{eff}(incl.) [GeV] >	1800	2200

Table 2: Selection criteria and targeted signal model used to define signal regions in the Meff-based search, indicated by the prefix 'Meff'. Each SR is labelled with the inclusive jet multiplicity considered ('2j', '3j' etc.) together with the degree of background rejection. The latter is denoted by the value corresponding to the m_{eff} cut. The $E_{\mathrm{T}}^{\mathrm{miss}}/m_{\mathrm{eff}}(N_{\mathrm{j}})$ cut in any N_{j}-jet channel uses a value of m_{eff} constructed from only the leading N_{j} jets ($m_{\mathrm{eff}}(N_{\mathrm{j}})$). However, the final m_{eff}(incl.) selection, which is used to define the signal regions, includes all jets with $p_{\mathrm{T}} > 50$ GeV.

7.2. The jets+$E_{\mathrm{T}}^{\mathrm{miss}}$ RJR-based search

As with the Meff-based search, various signal regions are defined in the RJR-based approach to be most sensitive to a variety of proposed signal hypotheses. It is chosen to limit the number of "scale variables" (those with units GeV) to only two when defining the signal regions targeting models with gluino- and squark-pair production. The various collections of signals are grouped according to sparticle mass splittings with dedicated optimizations. The two chosen scale variables are $H_{1,1}^{\mathrm{PP}}$ and either $H_{2,1}^{\mathrm{PP}}$ (for models targeting squark-pair production) or $H_{4,1}^{\mathrm{PP}}$ (for models targeting gluino-pair production). These serve to leverage events with large missing momentum and a high collective scale of visible objects in events. In order to further suppress SM backgrounds, a variety of additional constraints on unitless variables are imposed.

In general, the procedure follows that as the mass splitting between parent sparticle and LSP increases, the criteria applied to the scale variables are tightened, while the criteria on unitless variables are loosened. In searching for the squark-pair production, the overall balance of the events is studied with $H_{1,1}^{\mathrm{PP}}/H_{2,1}^{\mathrm{PP}}$. The range selected in this ratio aims to reject those events where the missing transverse momentum dominates the scale (upper requirement) and to ensure sufficient balance between the scales (lower requirement). The selection on the $p_{\mathrm{j2,\,T}}^{\mathrm{PP}}/H_{\mathrm{T\,2,1}}^{\mathrm{PP}}$ ratio serves to ensure that each of the jets contributes to the overall scale significantly. This particular ratio is a powerful criterion against imbalanced V+jets events, where one of the jets has a much higher momentum than the sub-leading jet. In order to protect against events where the z-component of the laboratory frame momentum dominates the scale, we select this ratio to be low.

For gluino-pair produced signals, the same principles are followed. Tight requirements are placed on $H_{1,1}^{\mathrm{PP}}/H_{4,1}^{\mathrm{PP}}$ and $H_{\mathrm{T\,4,1}}^{\mathrm{PP}}/H_{4,1}^{\mathrm{PP}}$ to target scenarios with compressed spectra. As with the squark case a ratio selection is used, on $p_{\mathrm{PP,\,z}}^{\mathrm{lab}}/\left(p_{\mathrm{PP,\,z}}^{\mathrm{lab}}+H_{\mathrm{T\,4,1}}^{\mathrm{PP}}\right)$ in this case, to test the size of the z-component relative to the overall scale. A lower threshold is placed on the ratio of the second jet divided by the scale of the hemisphere. This provides a very strong constraint against events where the two hemispheres are well-balanced but one of the jets dominates the scale variable contribution. As described in Section 5, the $|\frac{2}{3}\Delta\phi_{\mathrm{V,P}}^{\mathrm{PP}}-\frac{1}{3}\cos\theta_{\mathrm{p}}|$ variable serves to efficiently protect against high jet multiplicity events, mostly arising from top-quark processes, where the $E_{\mathrm{T}}^{\mathrm{miss}}$ would be mostly associated with a single hemisphere.

Additionally, separate SRs are defined for models with compressed spectra. Following the pattern of successive SRs targeting larger mass-splitting scenarios, several regions designed to be sensitive to various mass-splittings utilize the ISR-boosted compressed decay tree described in Section 5. These regions target mass-splittings from roughly 25 GeV to 200 GeV, in increasing order.

These variables in concert serve to provide criteria to reject each of the major backgrounds while efficiently maintaining signal candidates for the processes considered. In order to reject events where the $E_{\mathrm{T}}^{\mathrm{miss}}$ results from mis-measurements of jets, the $E_{\mathrm{T}}^{\mathrm{miss}}$ is associated with one or more jets using a transverse clustering scheme, identifying those jets which are closest in phase-space. The variable Δ_{QCD} considers the magnitude of $\boldsymbol{E}_{\mathrm{T}}^{\mathrm{miss}}$, the transverse momentum of the associated jets, along with the azimuthal angle between the two, in order to quantify the likelihood that mis-measurements of these jets were responsible for the $E_{\mathrm{T}}^{\mathrm{miss}}$. Multi-jet events with severe jet mis-measurements tend to have Δ_{QCD} values between [-1,0] while events with $E_{\mathrm{T}}^{\mathrm{miss}}$ from weakly-interacting particles prefer [0,1]. The variable is defined as the signed asymmetry between

- the transverse momentum of the associated jet system that projects onto the direction of the $E_{\mathrm{T}}^{\mathrm{miss}}$ system normalized to this value summed with the $E_{\mathrm{T}}^{\mathrm{miss}}$ and

- the normalized angle between this jet system and the vectoral sum of it and the $E_{\mathrm{T}}^{\mathrm{miss}}$ system.

The selection criteria of the resulting seventeen signal regions is summarized in Table 3. All signal regions corresponding to the RJR-based search have 'RJR' prefix.

Targeted signal	$\tilde{q}\tilde{q}, \tilde{q} \to q\tilde{\chi}_1^0$					
Requirement	Signal Region					
	RJR-S1		**RJR-S2**		**RJR-S3**	
$H_{1,1}^{\mathrm{PP}}/H_{2,1}^{\mathrm{PP}} \geq$	0.6		0.55		0.5	
$H_{1,1}^{\mathrm{PP}}/H_{2,1}^{\mathrm{PP}} \leq$	0.95		0.96		0.98	
$p_{\mathrm{PP,\,z}}^{\mathrm{lab}}/\left(p_{\mathrm{PP,\,z}}^{\mathrm{lab}} + H_{\mathrm{T}\,2,1}^{\mathrm{PP}}\right) \leq$	0.5		0.55		0.6	
$p_{\mathrm{j2,\,T}}^{\mathrm{PP}}/H_{\mathrm{T}\,2,1}^{\mathrm{PP}} \geq$	0.16		0.15		0.13	
$\Delta_{\mathrm{QCD}} >$	0.001					
	RJR-S1a	**RJR-S1b**	**RJR-S2a**	**RJR-S2b**	**RJR-S3a**	**RJR-S3b**
$H_{\mathrm{T}\,2,1}^{\mathrm{PP}}$ [GeV] >	1000	1200	1400	1600	1800	2000
$H_{1,1}^{\mathrm{PP}}$ [GeV] >	1000		1400		1600	

Targeted signal	$\tilde{g}\tilde{g}, \tilde{g} \to q\bar{q}\tilde{\chi}_1^0$					
Requirement	Signal Region					
	RJR-G1		**RJR-G2**		**RJR-G3**	
$H_{1,1}^{\mathrm{PP}}/H_{4,1}^{\mathrm{PP}} \geq$	0.35		0.25		0.2	
$H_{\mathrm{T}\,4,1}^{\mathrm{PP}}/H_{4,1}^{\mathrm{PP}} \geq$	0.8		0.75		0.65	
$p_{\mathrm{PP,\,z}}^{\mathrm{lab}}/\left(p_{\mathrm{PP,\,z}}^{\mathrm{lab}} + H_{\mathrm{T}\,4,1}^{\mathrm{PP}}\right) \leq$	0.5		0.55		0.6	
$\min\left(p_{\mathrm{j2\,T\,i}}^{\mathrm{PP}}/H_{\mathrm{T}\,2,1\,\mathrm{i}}^{\mathrm{PP}}\right) \geq$	0.12		0.1		0.08	
$\max\left(H_{1,\,0}^{\mathrm{Pi}}/H_{2,\,0}^{\mathrm{Pi}}\right) \leq$	0.95		0.97		0.98	
$\lvert\frac{2}{3}\Delta\phi_{\mathrm{V,P}}^{\mathrm{PP}} - \frac{1}{3}\cos\theta_{\mathrm{p}}\rvert \leq$	0.5		–			
$\Delta_{\mathrm{QCD}} >$	0					
	RJR-G1a	**RJR-G1b**	**RJR-G2a**	**RJR-G2b**	**RJR-G3a**	**RJR-G3b**
$H_{\mathrm{T}\,4,1}^{\mathrm{PP}}$ [GeV] >	1000	1200	1500	1900	2300	2800
$H_{1,1}^{\mathrm{PP}}$ [GeV] >	600		800		900	

Targeted signal	compressed spectra in $\tilde{q}\tilde{q}$ ($\tilde{q} \to q\tilde{\chi}_1^0$); $\tilde{g}\tilde{g}$ ($\tilde{g} \to q\bar{q}\tilde{\chi}_1^0$)				
Requirement	Signal Region				
	RJR-C1	**RJR-C2**	**RJR-C3**	**RJR-C4**	**RJR-C5**
$R_{\mathrm{ISR}} \geq$	0.9	0.85	0.8	0.75	0.70
$\Delta\phi_{\mathrm{ISR,\,I}} \geq$	3.1	3.07	2.95	2.95	2.95
$\Delta\phi(\mathrm{jet}_{1,2}, \boldsymbol{E}_{\mathrm{T}}^{\mathrm{miss}})_{\mathrm{min}} >$	-	-	-	0.4	0.4
M_{TS} [GeV] $\geq$	100	100	200	500	500
$p_{\mathrm{TS}}^{\mathrm{CM}}$ [GeV] $\geq$	800	800	600	600	600
$N_{\mathrm{jet}}^{\mathrm{V}} \geq$	1	1	2	2	3

Table 3: Selection criteria and targeted signal model used to define signal regions in the RJR-based search, indicated by the prefix 'RJR'. Each SR is labelled with the targeted SUSY particle or the targeted region of parameter space, such that 'S', 'G' and 'C' denote regions searching for squark-, gluino-pair production, or compressed spectra, respectively.

8. Background estimation

Standard Model background processes contribute to the event counts in the signal regions. The dominant sources in both searches presented here are: Z+jets, W+jets, top quark pairs, single top quarks, dibosons and multi-jet production. Non-collision backgrounds are negligible. Diboson production is estimated with MC simulated data normalized to NLO cross-section predictions, as described in Section 3. Most of the W+jets background is composed of $W \to \tau\nu$ events in which the τ-lepton decays to hadrons, with additional contributions from $W \to e\nu, \mu\nu$ events in which no baseline electron or muon is reconstructed. The largest part of the Z+jets background comes from the irreducible component in which $Z \to \nu\bar{\nu}$ decays generate large $E_{\mathrm{T}}^{\mathrm{miss}}$. Top quark pair production followed by semileptonic decays, in particular $t\bar{t} \to b\bar{b}\tau\nu qq'$ (with the τ-lepton decaying to hadrons), as well as single-top-quark events, can also generate large $E_{\mathrm{T}}^{\mathrm{miss}}$ and satisfy the jet and lepton-veto requirements. The multi-jet background in the signal regions is due to missing transverse momentum from misreconstruction of jet energies in the calorimeters, as well as neutrino production in semileptonic decays of heavy-flavour hadrons. After applying the requirements based on $\Delta\phi(\text{jet}, \boldsymbol{E}_{\mathrm{T}}^{\mathrm{miss}})_{\mathrm{min}}$ and $E_{\mathrm{T}}^{\mathrm{miss}}/m_{\mathrm{eff}}(N_{\mathrm{j}})$ in Meff-based search, or Δ_{QCD}, $p_{\mathrm{T}}^{\mathrm{PP}}/H_{\mathrm{T}\,2,1}^{\mathrm{PP}}$ and $\Delta\phi(\text{jet}, \boldsymbol{E}_{\mathrm{T}}^{\mathrm{miss}})_{\mathrm{min}}$ in RJR-based search, as indicated in Tables 2 and 3, the remaining multi-jet background is negligible.

8.1. Control regions

In order to estimate the backgrounds in a consistent and robust fashion, four control regions are defined for each of the signal regions for both searches. In the RJR-based search, a common set of CRs is used for all SRs in every targeted signal category (RJR-S, RJR-G or RJR-C). The CR selections are optimized to maintain the adequate statistical precision while minimizing the systematic uncertainties arising from the extrapolation of the CR event yield to estimate the background in the SR. This latter requirement is addressed through the use of CR jet p_{T} thresholds and m_{eff}(incl.) selections which match those used in the SR in the Meff-based search, and as close as possible selections based on RJR variables to the ones used in SRs in the RJR-based search. The basic CR definitions in both searches are listed in Table 4.

CR	SR background	CR process	CR selection (Meff-based)	CR selection (RJR-based)
Meff/RJR-CRγ	$Z(\to \nu\bar{\nu})$+jets	γ+jets	Isolated photon	Isolated photon
Meff/RJR-CRQ	Multi-jet	Multi-jet	SR with reversed requirements on (i) $\Delta\phi(\text{jet}, \boldsymbol{E}_{\mathrm{T}}^{\mathrm{miss}})_{\mathrm{min}}$ and (ii) $E_{\mathrm{T}}^{\mathrm{miss}}/m_{\mathrm{eff}}(N_{\mathrm{j}})$ or $E_{\mathrm{T}}^{\mathrm{miss}}/\sqrt{H_{\mathrm{T}}}$	$\Delta_{\mathrm{QCD}} < 0$ reversed requirement on $H_{1,1}^{\mathrm{PP}}$ (RJR-S/G) or $R_{\mathrm{ISR}} < 0.5$ (RJR-C)
Meff/RJR-CRW	$W(\to \ell\nu)$+jets	$W(\to \ell\nu)$+jets	30 GeV$< m_{\mathrm{T}}(\ell, E_{\mathrm{T}}^{\mathrm{miss}}) <$ 100 GeV, b-veto	
Meff/RJR-CRT	$t\bar{t}$(+EW) and single top	$t\bar{t} \to b\bar{b}qq'\ell\nu$	30 GeV$< m_{\mathrm{T}}(\ell, E_{\mathrm{T}}^{\mathrm{miss}}) <$ 100 GeV, b-tag	

Table 4: Control regions used in both searches presented in this document. Also listed are the main targeted background in the SR in each case, the process used to model the background, and the main CR requirement(s) used to select this process. The transverse momenta of high-purity leptons (photons) used to select CR events must exceed 27 (150) GeV. The jet p_{T} thresholds and m_{eff}(incl.) selections match those used in the corresponding SRs of Meff-based search. For the RJR-based search, selection based on the discriminating variables used for selecting SR events is described in the text.

The CRγ region in both searches (labelled as Meff/RJR-CRγ in Table 4) is used to estimate the contribution of $Z(\rightarrow \nu\bar{\nu})$+jets background events to each SR by selecting a sample of γ+jets events with $p_{\mathrm{T}}(\gamma) > 150$ GeV and then treating the reconstructed photon as invisible in the $E_{\mathrm{T}}^{\mathrm{miss}}$ calculation. For $p_{\mathrm{T}}(\gamma)$ significantly larger than m_Z the kinematic properties of such events strongly resemble those of Z+jets events [15]. In order to reduce the theoretical uncertainties associated with the Z/γ^*+jets background expectations in SRs arising from the use of LO γ+jets cross-sections, a correction factor is applied to the Meff/RJR-CRγ events. This correction factor, $\kappa = 1.39 \pm 0.05$, used in both searches, is determined by comparing Meff-CRγ observations with those in a highly populated auxiliary control region defined by selecting events with two electrons or muons for which the invariant mass lies within 25 GeV of the mass of the Z boson, satisfying $E_{\mathrm{T}}^{\mathrm{miss}} > 250$ GeV, $E_{\mathrm{T}}^{\mathrm{miss}}/\sqrt{H_{\mathrm{T}}} > 14$ GeV$^{1/2}$ and m_{eff}(incl.) > 800 GeV.

The CRW and CRT regions in both searches (labelled as Meff/RJR-CRW and Meff/RJR-CRT in Table 4) aim to select samples rich in $W(\rightarrow \ell\nu)$+jets and semileptonic $t\bar{t}$ background events respectively. They use events with one high-purity lepton with $p_{\mathrm{T}} > 27$ GeV and differ in their number of b-jets (zero or greater or equal to one respectively). In both searches, the requirement on the transverse mass m_{T} formed by the $E_{\mathrm{T}}^{\mathrm{miss}}$ and a selected lepton is applied, as indicated in Table 4. The lepton is treated as a jet with the same momentum to model background events in which a hadronically decaying τ-lepton is produced. The Meff-CRW and Meff-CRT selections omit the SR selection requirements on $\Delta\phi(\mathrm{jet}, \boldsymbol{E}_{\mathrm{T}}^{\mathrm{miss}})_{\mathrm{min}}$ and aplanarity for all SRs, while for the SRs requiring m_{eff}(incl.) > 2200 GeV the requirements on $E_{\mathrm{T}}^{\mathrm{miss}}/m_{\mathrm{eff}}(N_{\mathrm{j}})$ are not applied. This is done in order to increase the number of CR data events without significantly increasing the theoretical uncertainties associated with the background estimation procedure.

The multi-jet background in both searches is estimated using a data-driven technique [15], which applies a resolution function to well-measured multi-jet events in order to estimate the impact of jet energy mismeasurement and heavy-flavour semileptonic decays on $E_{\mathrm{T}}^{\mathrm{miss}}$ and other variables. The Meff-CRQ region uses reversed selection requirements on $\Delta\phi(\mathrm{jet}, \boldsymbol{E}_{\mathrm{T}}^{\mathrm{miss}})_{\mathrm{min}}$ and on $E_{\mathrm{T}}^{\mathrm{miss}}/m_{\mathrm{eff}}(N_{\mathrm{j}})$ (or $E_{\mathrm{T}}^{\mathrm{miss}}/\sqrt{H_{\mathrm{T}}}$ where appropriate) to produce samples enriched in multi-jet background events.

In the RJR-based search, all CRs corresponding to RJR-S (RJR-G) SRs are required to satisfy $H_{1,1}^{\mathrm{PP}} > 900$ (550) GeV . Additionally, $H_{\mathrm{T}\,2,1}^{\mathrm{PP}} > 1000$ GeV, $H_{\mathrm{T}\,4,1}^{\mathrm{PP}} > 800$ GeV and $M_{\mathrm{TS}} > 0$ GeV are required for RJR-CRW, RJR-CRT and RJR-CRQ, corresponding to RJR-S, RJR-G and RGR-C signal regions, respectively. In RJR-CRW and RJR-CRT, the requirements on all the other variables used for the RJR-SR selections are chosen such that the loosest value in the SR category (RJR-S, RJR-G or RJR-C) indicated in Table 3 is chosen. In RJR-CRQ corresponding to RJR-G signal regions $|\frac{2}{3}\Delta\phi_{\mathrm{V,P}}^{\mathrm{PP}} - \frac{1}{3}\cos\theta_{\mathrm{p}}| > 0.5$ is required in order to select events populated with the multi-jet background. No requirement on $p_{\mathrm{PP,\,z}}^{\mathrm{lab}}/\left(p_{\mathrm{PP,\,z}}^{\mathrm{lab}} + H_{\mathrm{T\,N,1}}^{\mathrm{PP}}\right)$ is used for the RJR-CRQ selections in all RJR-SRs.

As an example, the m_{eff}(incl.) distributions in control regions associated with Meff-4j-1000 selections are shown in Figure 3. Figure 4 shows the $p_{\mathrm{TS}}^{\mathrm{CM}}$ discriminant variable distributions in control regions corresponding to RJR-C1 signal region selections. In all CRs, the data are consistent with the pre-fit MC background prediction within uncertainties. The differences seen in the $p_{\mathrm{TS}}^{\mathrm{CM}}$ distribution for $p_{\mathrm{TS}}^{\mathrm{CM}} > 1200$ GeV in Figure 4(b) have negligible contribution to the overall normalization of the multi-jet background, which is expected to be negligible in the corresponding signal region, as presented in Figure 6 and Table 8.

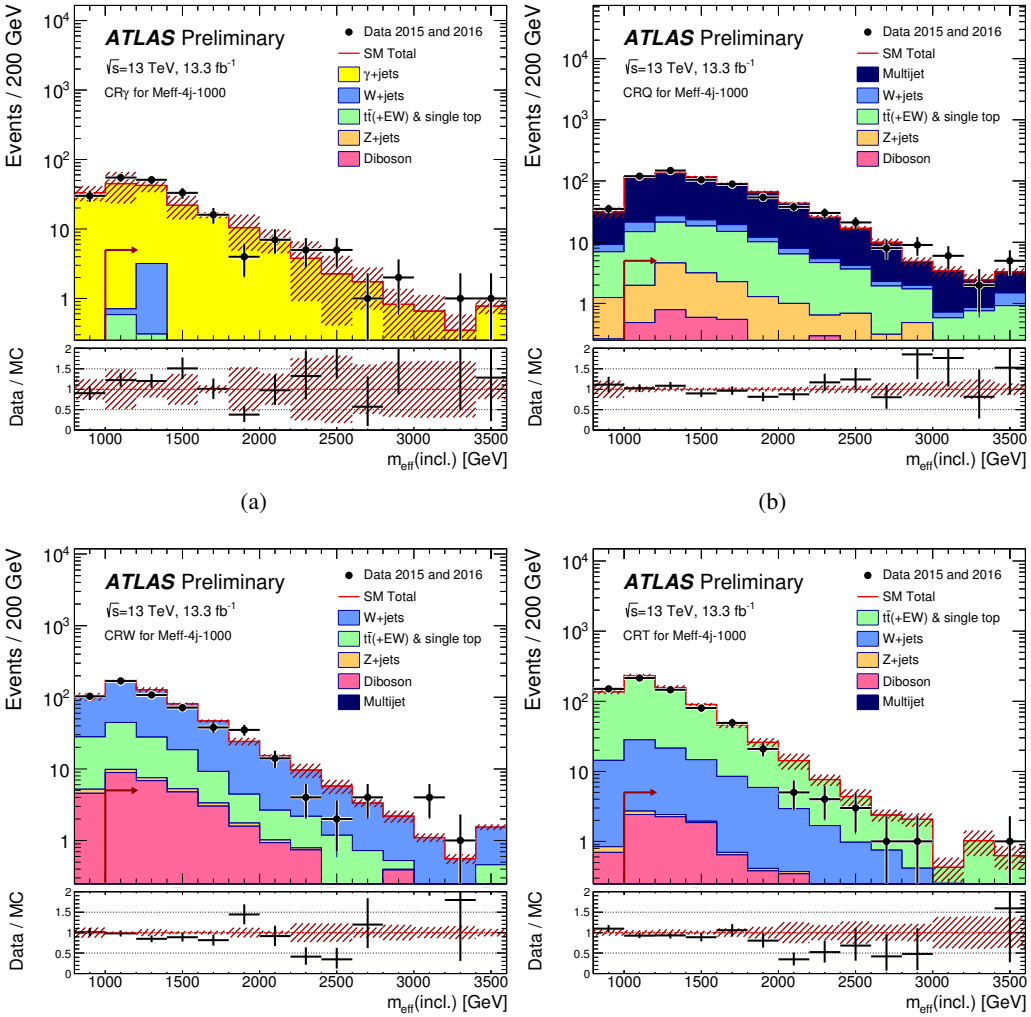

Figure 3: Observed m_{eff}(incl.) distributions in control regions (a) Meff-CRγ, (b) Meff-CRQ, (c) Meff-CRW and (d) Meff-CRT after selecting events with at least four energetic jets as indicated in Table 2 for Meff-4j-1000. No selection requirements on $\Delta\phi(\text{jet}, \boldsymbol{E}_{\text{T}}^{\text{miss}})_{\text{min}}$ are applied in Meff-CRW and Meff-CRT regions. The arrows indicate the values at which the requirements on m_{eff}(incl.) are applied. The histograms denote the pre-fit MC background expectations, normalized to cross-section times integrated luminosity. In case of γ+jets background, a κ factor described in the text is applied. The last bin includes the overflow. The hatched (red) error bands denote the combined experimental, MC statistical and theoretical modelling uncertainties.

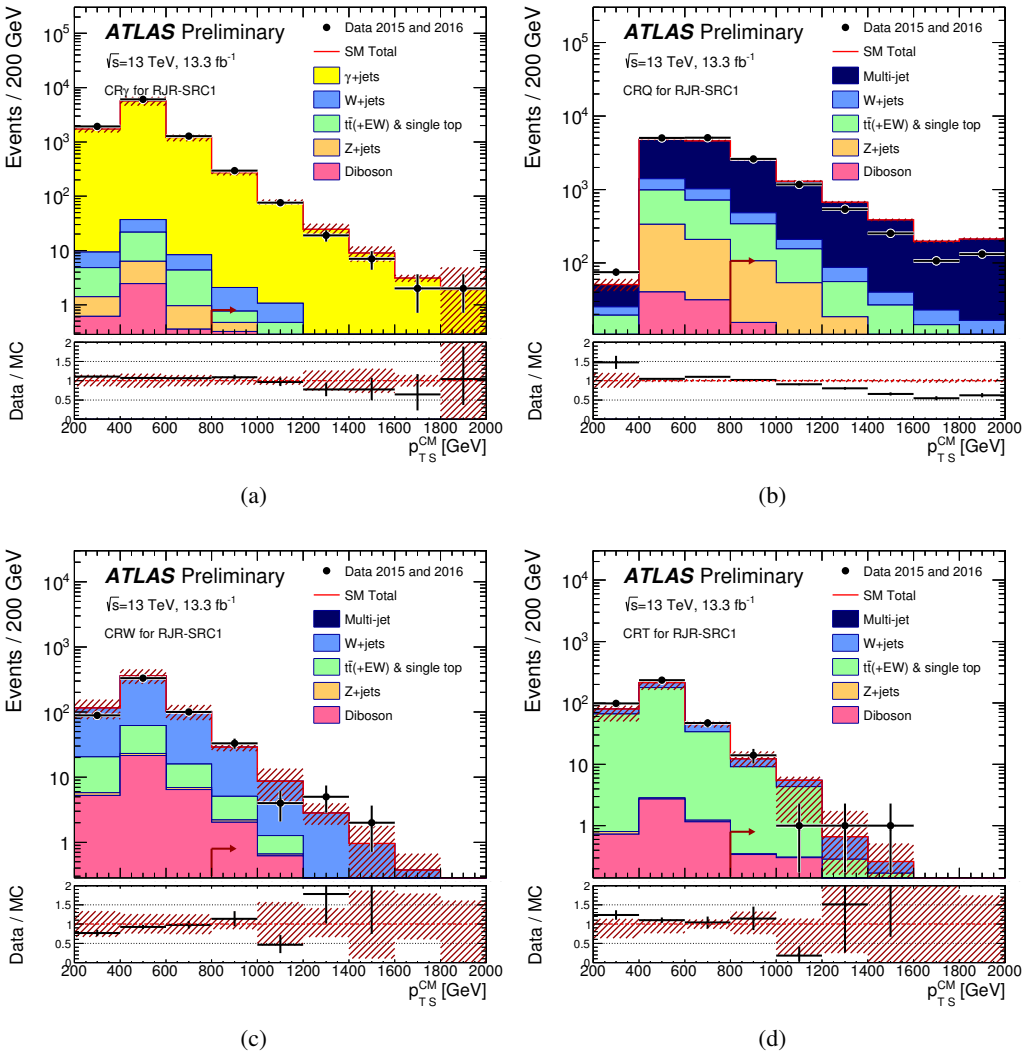

Figure 4: Observed $p_{\mathrm{TS}}^{\mathrm{CM}}$ distribution in control regions (a) RJR-CRγ, (b) RJR-CRQ, (c) RJR-CRW and (d) RJR-CRT after selecting events for the corresponding control regions as indicated in the text for RJR-C1 region and after applying all selection requirements except those on the plotted variable. The arrows indicate the values at which the requirements are applied. The histograms denote the pre-fit MC background expectations, normalized to cross-section times integrated luminosity. In case of γ+jets background, a κ factor described in the text is applied. The last bin includes the overflow. The hatched (red) error bands denote the combined experimental, MC statistical and theoretical modelling uncertainties.

8.2. Validation regions

The background estimation procedure is validated by comparing the numbers of events observed in the VRs to the corresponding SM background expectations obtained from the background-only fits. Several VR samples are selected in both searches, with requirements distinct from those used in the CRs, which maintain a low probability of signal contamination.

The Meff/RJR-CRγ estimates of the $Z(\rightarrow \nu\bar{\nu})$+jets background are validated using the samples of $Z(\rightarrow \ell\bar{\ell})$+jets events selected by requiring high-purity lepton pairs of opposite sign and identical flavour for which the dilepton invariant mass lies within 25 GeV of the mass of the Z boson (Meff/RJR-VRZ). In Meff/RJR-VRZ regions, the leptons are treated as contributing to $E_{\mathrm{T}}^{\mathrm{miss}}$. Additional VRs designed to validate the $Z(\rightarrow \ell\bar{\ell})$+jets estimation in RJR-based search are also used: VRZc region, which selects events with no leptons but requires inverted selection based on $\Delta\phi_{\mathrm{ISR,\,I}}$ requirement compared to the SR selection (Table 3) and VRZca, which on top of VRZc selection additionally applies looser set of requirements on SR discriminant variables, as listed for the RJR-CRW and RJR-CRT regions. In order to increase the statistics in RJR-VRZ regions, two additional regions, RJR-VRZa and RJR-VRZb are constructed with additionally loosened $H_{1,1}^{\mathrm{PP}}$ and $H_{\mathrm{T}\,2,1}^{\mathrm{PP}}$ (or $H_{\mathrm{T}\,4,1}^{\mathrm{PP}}$ where appropriate) to the values used for the RJR-CRW and RJR-CRT regions.

The Meff-CRW and Meff-CRT estimates of the W+jets and top quark background are validated with the same Meff-CRW and Meff-CRT selections, but reinstating the requirement on $\Delta\phi(\mathrm{jet}, \boldsymbol{E}_{\mathrm{T}}^{\mathrm{miss}})_{\mathrm{min}}$ and treating the lepton either as a jet (Meff-VRW, Meff-VRT) or as contributing to $E_{\mathrm{T}}^{\mathrm{miss}}$ (Meff-VRWν, Meff-VRTν). Similarly, the RJR-CRW and RJR-CRT estimates of the W+jets and top quark background are validated using the same selections as for the corresponding CRs, except that the requirements on $H_{1,1}^{\mathrm{PP}}$ and M_{TS} (RJR-VRWa, RJR-VRTa) or $H_{\mathrm{T}\,2,1}^{\mathrm{PP}}$ and $H_{\mathrm{T}\,4,1}^{\mathrm{PP}}$ (RJR-VRWb, RJR-VRTb) are omitted. Two additional VRs that require the presence of a high-purity lepton and either apply veto (RJR-VRW) or require the presence of at least one b-jet (RJR-VRT), and require no additional SR selection criteria, are also used in the analysis.

The Meff-CRQ estimates of the multi-jet background are validated with VRs for which the Meff-CRQ selection is applied, but with the SR $E_{\mathrm{T}}^{\mathrm{miss}}/m_{\mathrm{eff}}(N_{\mathrm{j}})$ ($E_{\mathrm{T}}^{\mathrm{miss}}/\sqrt{H_{\mathrm{T}}}$) requirement reinstated (Meff-VRQa), or with a requirement of an intermediate value of $\Delta\phi(\mathrm{jet}, \boldsymbol{E}_{\mathrm{T}}^{\mathrm{miss}})_{\mathrm{min}}$ applied (Meff-VRQb). For the RJR-VRQ region, the same selection as for the corresponding RJR-CRQ is used, except that the requirements on $H_{1,1}^{\mathrm{PP}}$, $H_{\mathrm{T}\,2,1}^{\mathrm{PP}}$ (or $H_{\mathrm{T}\,4,1}^{\mathrm{PP}}$ where appropriate) and M_{TS} are omitted depending on the region. Additional VRs with inverted Δ_{QCD} (RJR-VRQa), $H_{1,1}^{\mathrm{PP}}$ (RJR-VRQb) for RJR-S and RJR-G signal regions, and with $0.5 < R_{\mathrm{ISR}} <$ SR requirement for RJR-C regions (Table 3), are also used.

The results of the validation procedure are shown in Figure 5. Figure shows the differences in each VR between the numbers of observed and expected events expressed as fractions of the one-standard deviation (1σ) uncertainties on the latter. Most VR observations lie within 1σ of the background expectations for both searches, with the largest discrepancy being -2.3σ in the Meff-VRQa associated with the SR Meff-2j-2000 and in RJR-VRT associated with the SR RJR-C3 (1.9σ).

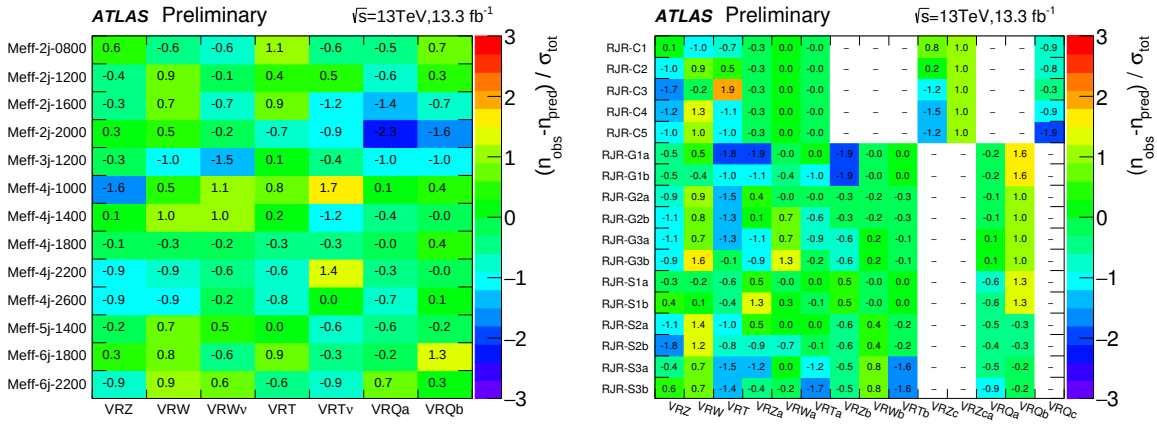

(a) (b)

Figure 5: Differences between the numbers of observed events in data and the SM background predictions for each VR used in the (a) Meff-based and (b) RJR-based search, expressed as a fraction of the total uncertainty which combines the uncertainty on the background expectations, and the expected statistical uncertainty of the test obtained from the number of expected events. Empty boxes (indicated by a '-') appear when VR is not used for the corresponding SR selection.

9. Systematic uncertainties

Systematic uncertainties in background estimates arise from the use of extrapolation factors which relate observations in the control regions to background expectations in the signal regions, and from the MC modelling of minor backgrounds.

The overall background uncertainties, detailed in Tables 5 and 6, range from 8% in SR Meff-2j-0800 and Meff-4j-1000 to 43% in SR Meff-6j-2200 and from 10% in SRs RJR-S1a, RJR-S2a, RJR-G1a, RJR-C2 and RJR-C3 to 24% in SR RJR-SRG3b.

For the backgrounds estimated with MC simulation-derived extrapolation factors, the primary common sources of systematic uncertainty are the jet energy scale (JES) calibration, jet energy resolution (JER), theoretical uncertainties, and limited event yields in the MC samples and data CRs. Correlations between uncertainties (for instance between JES or JER uncertainties in CRs and SRs) are taken into account where appropriate.

The JES uncertainty was measured using the techniques described in Refs. [83, 95, 96]. The JER uncertainty is estimated using the methods discussed in Refs. [83, 97]. An additional uncertainty in the modelling of energy not associated with reconstructed objects, used in the calculation of $E_{\mathrm{T}}^{\mathrm{miss}}$ and measured with unassociated charged tracks, is also included. The combined JES, JER and $E_{\mathrm{T}}^{\mathrm{miss}}$ (Jet/$E_{\mathrm{T}}^{\mathrm{miss}}$) uncertainty ranges from 1% of the expected background in 2-jet Meff-SRs to 12% in SR Meff-6j-2200. In RJR-based search, the same uncertainties range from 1% in RJR-S1 and RJR-S2 regions to 7% in RJR-SRC5.

Uncertainties arising from theoretical modelling of background processes are evaluated by comparing samples produced with different MC generators or by varying scale uncertainties. Uncertainties in the W/Z+jets production are estimated by increasing and decreasing the renormalization, factorization and resummation scales a factor of two, and by increasing and decreasing the nominal CKKW matching scale by 10 GeV and 5 GeV, respectively. Uncertainties in the modelling of top quark pair production are estimated by comparing Powheg-Box to MG5_aMC@NLO, and by accounting for different generator and radiation tunes. Uncertainties associated with PDF modelling of top quark pair production are found to be negligible. Uncertainties in diboson production due to PDF, renormalization, factorization and resummation scale uncertainties (estimated by increasing and decreasing the scales used in the MC generators by a factor of two) are accounted for by applying a uniform 50% uncertainty in all SRs, and range from 2% in Meff-2j-0800 and Meff-4j-2600 to 9% in SR 6-jet Meff-SRs. In RJR-based search, the same uncertainties range from 3% in RJR-S1 and RJR-S2 regions to 8% in RJR-SRG3b. Uncertainties associated with the modelling of Z+jets production are largest in the 2-jet Meff-SRs (7%). In the RJR-based search, these uncertainties are maximal in RJR-SRS2b and RJR-SRS3b SR (8%).

The uncertainties arising from the data-driven correction procedure applied to events selected in the CRγ region, described in Section 8, are included in Tables 5 and 6 under 'CRγ corr. factor' and reach a value of 2% in most of the Meff-SRs, except in the Meff-2j-0800, Meff-2j-1200 and Meff-2j-2000 SRs where it reaches the maximal value of 14%. The same uncertainty in the RJR-based search ranges from 2% in SRs RJR-C3 and RJR-SRC5 to 4% in most RJR-S SRs.

Uncertainties related to the multi-jet background estimates are accounted for by applying a uniform 100% uncertainty in all SRs. In most of the SRs these uncertainties are negligible, and the maximum resulting contribution to the overall background uncertainty is 1% in SR Meff-4j-1400. In RJR-based search, this uncertainty is $< 1\%$ or negligible in most regions, and reaches maximal value of 5% in RJR-G2b.

The statistical uncertainty arising from the use of MC samples is largest in SRs Meff-6j-2200 (20%) and RJR-SRG3b (14%).

The impact of lepton reconstruction uncertainties, and of the uncertainties related to the b-tag/b-veto efficiency, on the overall background uncertainty are found to be negligible for all SRs.

The total background uncertainties for SRs used in both searches presented in this document, broken down into the main contributing sources, are summarized in Tables 5 and 6.

Channel	**Meff-2j-0800**	**Meff-2j-1200**	**Meff-2j-1600**	**Meff-2j-2000**	**Meff-3j-1200**
Total bkg	610	297	121	42	355
Total bkg unc.	±50 [8%]	±29 [10%]	±13 [11%]	±6 [14%]	±33 [9%]
MC statistics	–	±3.1 [1%]	±1.8 [1%]	±1.0 [2%]	±4 [1%]
$\Delta\mu_{Z+\text{jets}}$	±12 [2%]	±8 [3%]	±5 [4%]	±2.9 [7%]	±9 [3%]
$\Delta\mu_{W+\text{jets}}$	±9 [1%]	±8 [3%]	±5 [4%]	±2.5 [6%]	±8 [2%]
$\Delta\mu_{\text{Top}}$	±5 [1%]	±3.5 [1%]	±2.2 [2%]	±0.21 [1%]	±7 [2%]
$\Delta\mu_{\text{Multi-jet}}$	±0.04 [0%]	±0.1 [0%]	–	–	±0.03 [0%]
CRγ corr. factor	±22 [4%]	±11 [4%]	±4 [3%]	±1.5 [4%]	±11 [3%]
Theory Z	±40 [7%]	±22 [7%]	±9 [7%]	±3.0 [7%]	±22 [6%]
Theory W	±0.32 [0%]	±3.1 [1%]	±1.0 [1%]	±1.2 [3%]	±0.7 [0%]
Theory Top	±3.4 [1%]	±0.6 [0%]	±0.6 [0%]	±0.24 [1%]	±4 [1%]
Theory Diboson	±14 [2%]	±8 [3%]	±4 [3%]	±1.9 [5%]	±16 [5%]
Jet/MET	±5 [1%]	±2.8 [1%]	±1.8 [1%]	±0.28 [1%]	±4 [1%]
Multi-jet method	±1.6 [0%]	±0.4 [0%]	–	–	±0.6 [0%]

Channel	**Meff-4j-1000**	**Meff-4j-1400**	**Meff-4j-1800**	**Meff-4j-2200**	**Meff-4j-2600**	**Meff-5j-1400**
Total bkg	84	66	27.0	4.8	2.7	68
Total bkg unc.	±7 [8%]	±8 [12%]	±3.2 [12%]	±1.1 [23%]	±0.6 [22%]	±9 [13%]
MC statistics	±2.6 [3%]	±1.8 [3%]	±1.1 [4%]	±0.35 [7%]	±0.32 [12%]	±2.3 [3%]
$\Delta\mu_{Z+\text{jets}}$	±3.1 [4%]	±3.0 [5%]	±1.4 [5%]	±0.4 [8%]	±0.23 [9%]	±3.2 [5%]
$\Delta\mu_{W+\text{jets}}$	±1.9 [2%]	±2.0 [3%]	±1.1 [4%]	±0.27 [6%]	±0.4 [15%]	±4 [6%]
$\Delta\mu_{\text{Top}}$	±2.6 [3%]	±1.6 [2%]	±0.9 [3%]	±0.16 [3%]	±0.11 [4%]	±4 [6%]
$\Delta\mu_{\text{Multi-jet}}$	±0.03 [0%]	±0.02 [0%]	–	–	–	±0.02 [0%]
CRγ corr. factor	±1.9 [2%]	±1.9 [3%]	±0.7 [3%]	±0.13 [3%]	±0.06 [2%]	±1.6 [2%]
Theory Z	±4 [5%]	±4 [6%]	±1.4 [5%]	±0.27 [6%]	±0.13 [5%]	±3.3 [5%]
Theory W	±1.3 [2%]	±0.7 [1%]	±0.24 [1%]	±0.06 [1%]	±0.26 [10%]	±2.1 [3%]
Theory Top	±1.3 [2%]	±3.2 [5%]	±0.9 [3%]	±0.5 [10%]	±0.16 [6%]	±3.2 [5%]
Theory Diboson	±2.1 [3%]	±2.8 [4%]	±1.5 [6%]	±0.4 [8%]	±0.06 [2%]	±4 [6%]
Jet/MET	±2.0 [2%]	±1.6 [2%]	±0.34 [1%]	±0.11 [2%]	±0.09 [3%]	±0.6 [1%]
Multi-jet method	±0.32 [0%]	±0.32 [0%]	–	–	–	±0.16 [0%]

Channel	**Meff-6j-1800**	**Meff-6j-2200**
Total bkg	5.5	0.82
Total bkg unc.	±1.0 [18%]	±0.35 [43%]
MC statistics	±0.6 [11%]	±0.16 [20%]
$\Delta\mu_{Z+\text{jets}}$	±0.4 [7%]	±0.11 [13%]
$\Delta\mu_{W+\text{jets}}$	±0.31 [6%]	±0.12 [15%]
$\Delta\mu_{\text{Top}}$	±0.4 [7%]	±0.1 [12%]
$\Delta\mu_{\text{Multi-jet}}$	–	–
CRγ corr. factor	±0.1 [2%]	±0.02 [2%]
Theory Z	±0.21 [4%]	±0.04 [5%]
Theory W	±0.09 [2%]	±0.04 [5%]
Theory Top	±0.31 [6%]	±0.21 [26%]
Theory Diboson	±0.5 [9%]	±0.07 [9%]
Jet/MET	±0.12 [2%]	±0.1 [12%]
Multi-jet method	–	–

Table 5: Breakdown of the dominant systematic uncertainties in the background estimates for the Meff-based search. The individual uncertainties can be correlated, and do not necessarily add in quadrature to the total background uncertainty. $\Delta\mu$ uncertainties are the result of the control region statistical uncertainties and the systematic uncertainties entering a specific control region. In brackets, uncertainties are given relative to the expected total background yield, also presented in the Table. Empty cells (indicated by a '-') correspond to uncertainties <0.1%.

Channel	**RJR-S1a**	**RJR-S1b**	**RJR-S2a**	**RJR-S2b**	**RJR-S3a**	**RJR-S3b**
Total bkg	334	233	96	75	56	37
Total bkg unc.	±35 [10%]	±25 [11%]	±10 [10%]	±8 [11%]	±6 [11%]	±4 [11%]
MC statistics	–	±2.6 [1%]	±1.5 [2%]	±1.3 [2%]	±1.0 [2%]	±0.7 [2%]
$\Delta\mu_{Z+\text{jets}}$	±20 [6%]	±14 [6%]	±4 [4%]	±2.9 [4%]	±2.2 [4%]	±1.5 [4%]
$\Delta\mu_{W+\text{jets}}$	±10 [3%]	±7 [3%]	±3.1 [3%]	±2.3 [3%]	±1.6 [3%]	±1.1 [3%]
$\Delta\mu_{\text{Top}}$	±6 [2%]	±4 [2%]	±1.5 [2%]	±1.1 [1%]	±0.9 [2%]	±0.6 [2%]
$\Delta\mu_{\text{Multi-jet}}$	±0.09 [0%]	±0.05 [0%]	±0.02 [0%]	–	–	–
CRγ corr. factor	±12 [4%]	±8 [3%]	±4 [4%]	±2.9 [4%]	±2.2 [4%]	±1.4 [4%]
Theory Z	±23 [7%]	±16 [7%]	±7 [7%]	±6 [8%]	±4 [7%]	±2.8 [8%]
Theory W	±4 [1%]	±5 [2%]	±0.4 [0%]	±0.11 [0%]	±1.5 [3%]	±1.2 [3%]
Theory Top	±4 [1%]	±2.7 [1%]	±0.8 [1%]	±0.7 [1%]	±0.6 [1%]	±0.4 [1%]
Theory Diboson	±9 [3%]	±6 [3%]	±2.8 [3%]	±2.6 [3%]	±2.1 [4%]	±1.4 [4%]
Jet/MET	±3.3 [1%]	±1.5 [1%]	±0.6 [1%]	±0.6 [1%]	±1.2 [2%]	±1.0 [3%]
Multi-jet method	±0.7 [0%]	±0.4 [0%]	±0.08 [0%]	–	–	–

Channel	**RJR-G1a**	**RJR-G1b**	**RJR-G2a**	**RJR-G2b**	**RJR-G3a**	**RJR-G3b**
Total bkg	40	18.8	27.8	8.5	5.8	1.7
Total bkg unc.	±4 [10%]	±2.5 [13%]	±3.4 [12%]	±1.4 [16%]	±1.1 [19%]	±0.4 [24%]
MC statistics	±1.6 [4%]	±1.0 [5%]	±1.2 [4%]	±0.6 [7%]	±0.4 [7%]	±0.23 [14%]
$\Delta\mu_{Z+\text{jets}}$	±1.5 [4%]	±0.7 [4%]	±1.6 [6%]	±0.5 [6%]	±0.4 [7%]	±0.1 [6%]
$\Delta\mu_{W+\text{jets}}$	±0.9 [2%]	±0.4 [2%]	±1.2 [4%]	±0.31 [4%]	±0.28 [5%]	±0.1 [6%]
$\Delta\mu_{\text{Top}}$	±0.8 [2%]	±0.33 [2%]	±0.9 [3%]	±0.23 [3%]	±0.07 [1%]	±0.1 [6%]
$\Delta\mu_{\text{Multi-jet}}$	±0.1 [0%]	–	±0.03 [0%]	±0.02 [0%]	–	–
CRγ corr. factor	±1.2 [3%]	±0.6 [3%]	±0.8 [3%]	±0.26 [3%]	±0.19 [3%]	±0.05 [3%]
Theory Z	±2.3 [6%]	±1.1 [6%]	±1.6 [6%]	±0.5 [6%]	±0.4 [7%]	±0.1 [6%]
Theory W	±1.1 [3%]	±1.3 [7%]	±0.3 [1%]	±0.7 [8%]	±0.6 [10%]	±0.16 [9%]
Theory Top	±1.2 [3%]	±0.7 [4%]	±1.0 [4%]	±0.4 [5%]	±0.4 [7%]	±0.26 [15%]
Theory Diboson	±1.3 [3%]	±0.8 [4%]	±1.5 [5%]	±0.6 [7%]	±0.31 [5%]	±0.13 [8%]
Jet/MET	±1.0 [3%]	±0.6 [3%]	±0.4 [1%]	±0.17 [2%]	±0.22 [4%]	±0.05 [3%]
Multi-jet method	±0.24 [1%]	±0.12 [1%]	±0.5 [2%]	±0.4 [5%]	–	–

Channel	**RJR-C1**	**RJR-C2**	**RJR-C3**	**RJR-C4**	**RJR-C5**
Total bkg	14.5	59	110	10.5	7.3
Total bkg unc.	±2.2 [15%]	±6 [10%]	±11 [10%]	±1.5 [14%]	±1.4 [19%]
MC statistics	±0.7 [5%]	±1.7 [3%]	±2.4 [2%]	±0.6 [6%]	±0.6 [8%]
$\Delta\mu_{Z+\text{jets}}$	±0.5 [3%]	±1.9 [3%]	±2.5 [2%]	±0.31 [3%]	±0.13 [2%]
$\Delta\mu_{W+\text{jets}}$	±0.4 [3%]	±1.7 [3%]	±5 [5%]	±0.4 [4%]	±0.25 [3%]
$\Delta\mu_{\text{Top}}$	±0.33 [2%]	±1.3 [2%]	±4 [4%]	±0.31 [3%]	±0.4 [5%]
$\Delta\mu_{\text{Multi-jet}}$	–	±0.1 [0%]	±0.06 [0%]	–	±0.1 [1%]
CRγ corr. factor	±0.5 [3%]	±1.8 [3%]	±2.3 [2%]	±0.29 [3%]	±0.13 [2%]
Theory Z	±0.8 [6%]	±3.5 [6%]	±4 [4%]	±0.6 [6%]	±0.24 [3%]
Theory W	±1.3 [9%]	±0.03 [0%]	±2.0 [2%]	±1.0 [10%]	±0.13 [2%]
Theory Top	±0.5 [3%]	±1.3 [2%]	±3.2 [3%]	±0.6 [6%]	±0.9 [12%]
Theory Diboson	±1.0 [7%]	±4 [7%]	±6 [5%]	±0.27 [3%]	±0.4 [5%]
Jet/MET	±0.5 [3%]	±1.5 [3%]	±3.1 [3%]	±0.24 [2%]	±0.5 [7%]
Multi-jet method	±0.09 [1%]	±0.4 [1%]	±2.1 [2%]	–	±0.18 [2%]

Table 6: Breakdown of the dominant systematic uncertainties in the background estimates for the RJR-based search. The individual uncertainties can be correlated, and do not necessarily add in quadrature to the total background uncertainty. $\Delta\mu$ uncertainties are the result of the control region statistical uncertainties and the systematic uncertainties entering a specific control region. In brackets, uncertainties are given relative to the expected total background yield, also presented in the Table. Empty cells (indicated by a '-') correspond to uncertainties <0.1%.

10. Results, interpretation and limits

The number of events observed in the data and the number of SM events expected to enter each of the signal regions, determined using the background-only fit, are shown in Tables 7 and 8 and in Figure 6. The pre-fit background expectations are also shown in Tables 7 and 8 for comparison.

The fit to the CRs for each SR compensates for the differences related to the overall normalization of the background seen in Figures 7 and 8, leading to good agreement between data and post-fit expectations in most of the the SRs. The most significant observed excess across the thirty signal regions for both searches, with a p-value for the background-only hypothesis of 0.01, corresponding to a significance of 1.56 standard deviations, occurs in SR Meff-6j-1800 (Table 7).

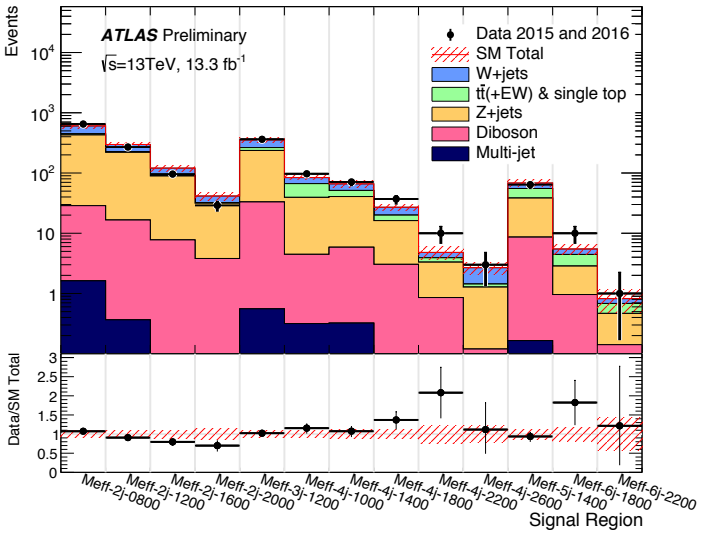

(a)

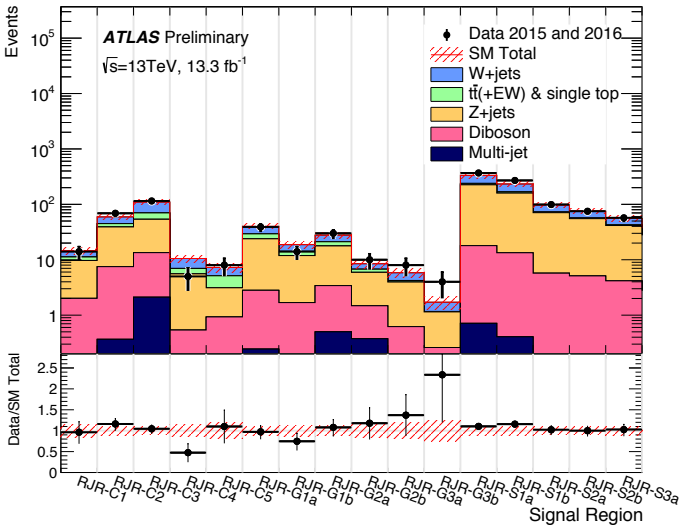

(b)

Figure 6: Comparison of the observed and expected event yields as a function of signal region in the (a) Meff-based and (b) RJR-based search. The background expectations are those obtained from the background-only fits, presented in Table 7.

Signal Region	**Meff-2j-0800**	**Meff-2j-1200**	**Meff-2j-1600**	**Meff-2j-2000**	**Meff-3j-1200**
MC expected events					
Diboson	27	16	7.8	3.8	35
Z/γ^*+jets	365	183	70	24	219
W+jets	161	73	24	7.7	95
$t\bar{t}$(+EW) + single top	30	10	3.7	1.5	41
Fitted background events					
Diboson	27 ± 14	16 ± 8	8 ± 4	3.8 ± 1.9	33 ± 16
Z/γ^*+jets	400 ± 50	204 ± 26	81 ± 11	28 ± 5	204 ± 27
W+jets	154 ± 11	71 ± 10	29 ± 4	9.3 ± 3.4	91 ± 8
$t\bar{t}$(+EW) + single top	23 ± 5	6 ± 4	2.5 ± 2.3	0.7 ± 0.5	27 ± 10
Multi-jet	1.6 ± 1.6	0.4 ± 0.4	–	–	0.6 ± 0.6
Total Expected MC	584	283	106	37	387
Total Fitted bkg	610 ± 50	297 ± 29	121 ± 13	42 ± 6	355 ± 33
Observed	650	270	96	29	363
$\langle \epsilon\sigma \rangle^{95}_{\rm obs}$ [fb]	11	3.7	1.4	0.73	6.0
$S^{95}_{\rm obs}$	146	49	19	9.7	78
$S^{95}_{\rm exp}$	115^{+42}_{-32}	63^{+22}_{-17}	30^{+12}_{-8}	$15.9^{+6.5}_{-4.6}$	74^{+27}_{-20}
p_0 (Z)	0.23 (0.75)	0.50 (0.00)	0.50 (0.00)	0.50 (0.00)	0.42 (0.21)

Signal Region	**Meff-4j-1000**	**Meff-4j-1400**	**Meff-4j-1800**	**Meff-4j-2200**	**Meff-4j-2600**	**Meff-5j-1400**
MC expected events						
Diboson	4.2	5.5	3.0	0.86	0.12	8.0
Z/γ^*+jets	29	34	14	2.7	1.3	37
W+jets	20	16	6.6	1.4	1.1	23
$t\bar{t}$(+EW) + single top	31	14	6.7	0.88	0.48	21
Fitted background events						
Diboson	4.2 ± 2.1	5.5 ± 2.8	3.0 ± 1.5	0.9 ± 0.4	0.12 ± 0.06	8 ± 4
Z/γ^*+jets	35 ± 5	35 ± 5	13.2 ± 2.2	2.5 ± 0.5	1.16 ± 0.31	30 ± 5
W+jets	17.4 ± 2.5	14.7 ± 2.1	7.0 ± 1.2	0.89 ± 0.29	1.3 ± 0.5	13 ± 4
$t\bar{t}$(+EW) + single top	27.2 ± 3.3	11 ± 5	3.8 ± 1.4	$0.61^{+0.85}_{-0.61}$	$0.16^{+0.21}_{-0.16}$	17 ± 6
Multi-jet	0.32 ± 0.32	0.32 ± 0.32	–	–	–	$0.17^{+0.17}_{-0.17}$
Total Expected MC	85	70	31	5.8	3.1	89
Total Fitted bkg	84 ± 7	66 ± 8	27.0 ± 3.2	4.8 ± 1.1	2.7 ± 0.6	68 ± 9
Observed	97	71	37	10	3	64
$\langle \epsilon\sigma \rangle^{95}_{\rm obs}$ [fb]	2.6	1.9	1.7	0.89	0.38	1.6
$S^{95}_{\rm obs}$	35	26	22	12	5.1	22
$S^{95}_{\rm exp}$	24^{+10}_{-7}	23^{+8}_{-6}	14^{+6}_{-4}	$7.9^{+3.5}_{-2.3}$	$4.8^{+2.6}_{-1.6}$	24^{+9}_{-7}
p_0 (Z)	0.14 (1.06)	0.34 (0.41)	0.06 (1.53)	0.07 (1.50)	0.43 (0.18)	0.50 (0.00)

Signal Region	**Meff-6j-1800**	**Meff-6j-2200**
MC expected events		
Diboson	0.96	0.14
Z/γ^*+jets	2.7	0.42
W+jets	1.38	0.29
$t\bar{t}$(+EW) + single top	2.8	0.42
Fitted background events		
Diboson	1.0 ± 0.5	0.14 ± 0.08
Z/γ^*+jets	1.9 ± 0.5	0.33 ± 0.13
W+jets	1.04 ± 0.35	0.14 ± 0.13
$t\bar{t}$(+EW) + single top	1.6 ± 0.5	$0.22^{+0.26}_{-0.22}$
Multi-jet	–	–
Total Expected MC	8	1.3
Total Fitted bkg	5.5 ± 1.0	0.82 ± 0.35
Observed	10	1
$\langle \epsilon\sigma \rangle^{95}_{\rm obs}$ [fb]	0.83	0.27
$S^{95}_{\rm obs}$	11	3.5
$S^{95}_{\rm exp}$	$6.5^{+3.3}_{-2.1}$	$3.3^{+2.1}_{-1.3}$
p_0 (Z)	0.06 (1.56)	0.43 (0.17)

Table 7: Numbers of events observed in the signal regions used in the Meff-based analysis compared with background expectations obtained from the fits described in the text. Empty cells (indicated by a '-') correspond to estimates lower than 0.01. The p-values (p_0) give the probabilities of the observations being consistent with the estimated backgrounds. For an observed number of events lower than expected, the p-value is truncated at 0.5. Between parentheses, p-values are also given as the number of equivalent Gaussian standard deviations (Z). Also shown are 95% CL upper limits on the visible cross-section ($\langle \epsilon\sigma \rangle^{95}_{\rm obs}$), the visible number of signal events ($S^{95}_{\rm obs}$) and the number of signal events ($S^{95}_{\rm exp}$) given the expected number of background events (and $\pm 1\sigma$ excursions of the expectation).

Signal Region	RJR-S1a	RJR-S1b	RJR-S2a	RJR-S2b	RJR-S3a	RJR-S3b
MC expected events						
Diboson	17	13	5.6	5.1	4.2	2.8
Z/γ^*+jets	231	163	63	48	36	24
W+jets	97	66	22	16	11	7.8
$t\bar{t}$(+EW) + single top	15	10	2.9	2.1	1.7	1.1
Fitted background events						
Diboson	17 ± 9	13 ± 7	5.6 ± 2.8	5.1 ± 2.6	4.2 ± 2.1	2.8 ± 1.4
Z/γ^*+jets	207 ± 33	146 ± 23	65 ± 9	50 ± 7	37 ± 5	25.0 ± 3.5
W+jets	95 ± 9	65 ± 7	24.1 ± 2.9	18.3 ± 2.3	12.8 ± 2.8	8.7 ± 2.0
$t\bar{t}$(+EW) + single top	14 ± 7	9 ± 5	2.1 ± 1.7	1.6 ± 1.3	1.3 ± 1.0	0.8 ± 0.7
Multi-jet	$0.71^{+0.71}_{-0.71}$	$0.41^{+0.41}_{-0.41}$	$0.08^{+0.09}_{-0.08}$	–	–	–
Total Expected MC	362	253	93	72	53	36
Total Fitted bkg	334 ± 35	233 ± 25	96 ± 10	75 ± 8	56 ± 6	37 ± 4
Observed	368	270	99	75	57	36
$\langle \epsilon\sigma \rangle^{95}_{\rm obs}$ [fb]	7.6	6.5	2.2	1.7	1.6	1.1
$S^{95}_{\rm obs}$	101	86	29	23	22	15
$S^{95}_{\rm exp}$	78^{+27}_{-21}	61^{+22}_{-16}	28^{+11}_{-8}	23^{+9}_{-7}	20^{+8}_{-6}	16^{+7}_{-5}
p_0 (Z)	0.20 (0.84)	0.12 (1.17)	0.44 (0.15)	0.50 (0.00)	0.44 (0.14)	0.50 (0.00)

Signal Region	RJR-G1a	RJR-G1b	RJR-G2a	RJR-G2b	RJR-G3a	RJR-G3b
MC expected events						
Diboson	2.6	1.6	2.9	1.1	0.62	0.26
Z/γ^*+jets	18	8.8	13	4.2	3.1	0.83
W+jets	11	4.7	7.7	2.0	1.9	0.63
$t\bar{t}$(+EW) + single top	7.4	3.1	4.4	1.1	0.34	0.03
Fitted background events						
Diboson	2.6 ± 1.3	1.6 ± 0.8	2.9 ± 1.5	1.1 ± 0.6	0.6 ± 0.4	0.26 ± 0.14
Z/γ^*+jets	21.1 ± 3.1	10.2 ± 1.6	14.3 ± 2.5	4.5 ± 0.8	3.3 ± 0.6	0.88 ± 0.19
W+jets	10.8 ± 1.7	4.6 ± 1.4	6.7 ± 1.3	1.7 ± 0.7	1.6 ± 0.7	0.55 ± 0.2
$t\bar{t}$(+EW) + single top	5.4 ± 1.6	2.3 ± 0.9	3.4 ± 1.4	0.8 ± 0.5	$0.26^{+0.45}_{-0.26}$	$0.02^{+0.26}_{-0.02}$
Multi-jet	0.24 ± 0.24	0.12 ± 0.12	0.5 ± 0.5	0.4 ± 0.4	–	–
Total Expected MC	39	18	29	8.7	5.9	1.7
Total Fitted bkg	40 ± 4	18.8 ± 2.5	27.8 ± 3.4	8.5 ± 1.4	5.8 ± 1.1	1.7 ± 0.4
Observed	39	14	30	10	8	4
$\langle \epsilon\sigma \rangle^{95}_{\rm obs}$ [fb]	1.1	0.56	1.1	0.71	0.64	0.55
$S^{95}_{\rm obs}$	15	7.5	15	9.4	8.5	7.3
$S^{95}_{\rm exp}$	16^{+7}_{-4}	10^{+5}_{-3}	14^{+6}_{-4}	$7.6^{+3.5}_{-2.0}$	$7.0^{+2.5}_{-2.1}$	$4.2^{+1.9}_{-0.5}$
p_0 (Z)	0.50 (0.00)	0.50 (0.00)	0.36 (0.35)	0.31 (0.50)	0.21 (0.81)	0.06 (1.55)

Signal Region	RJR-C1	RJR-C2	RJR-C3	RJR-C4	RJR-C5
MC expected events					
Diboson	1.9	7.1	11	0.54	0.75
Z/γ^*+jets	8.8	36	46	5.8	2.5
W+jets	3.5	16	43	3.8	2.3
$t\bar{t}$(+EW) + single top	1.9	7.2	20	1.7	2.5
Fitted background events					
Diboson	1.9 ± 1.0	7 ± 4	11 ± 6	0.54 ± 0.29	0.8 ± 0.5
Z/γ^*+jets	7.7 ± 1.1	32 ± 5	40 ± 6	5.0 ± 0.8	2.2 ± 0.4
W+jets	3.3 ± 1.4	14.5 ± 1.7	40 ± 5	3.56 ± 1.0	2.14 ± 0.35
$t\bar{t}$(+EW) + single top	1.5 ± 0.6	5.8 ± 1.8	16 ± 5	1.4 ± 0.7	2.0 ± 1.1
Multi-jet	0.09 ± 0.09	0.4 ± 0.4	2.1 ± 2.1	–	0.18 ± 0.18
Total Expected MC	16	67	124	12	8.3
Total Fitted bkg	14.5 ± 2.2	59 ± 6	110 ± 11	10.5 ± 1.5	7.3 ± 1.4
Observed	14	69	115	5	8
$\langle \epsilon\sigma \rangle^{95}_{\rm obs}$ [fb]	0.76	2.2	2.5	0.35	0.61
$S^{95}_{\rm obs}$	10	29	34	4.7	8.1
$S^{95}_{\rm exp}$	11^{+5}_{-3}	21^{+9}_{-6}	30^{+12}_{-8}	$8.1^{+3.0}_{-2.3}$	$7.4^{+2.9}_{-1.8}$
p_0 (Z)	0.50 (0.00)	0.18 (0.92)	0.37 (0.32)	0.50 (0.00)	0.39 (0.30)

Table 8: Numbers of events observed in the signal regions used in the RJR-based analysis compared with background expectations obtained from the fits described in the text. Empty cells (indicated by a '-') correspond to estimates lower than 0.01. The p-values (p_0) give the probabilities of the observations being consistent with the estimated backgrounds. For an observed number of events lower than expected, the p-value is truncated at 0.5. Between parentheses, p-values are also given as the number of equivalent Gaussian standard deviations (Z). Also shown are 95% CL upper limits on the visible cross-section ($\langle \epsilon\sigma \rangle^{95}_{\rm obs}$), the visible number of signal events ($S^{95}_{\rm obs}$) and the number of signal events ($S^{95}_{\rm exp}$) given the expected number of background events (and $\pm 1\sigma$ excursions of the expectation).

Distributions of m_{eff}(incl.) from the Meff-based search for selected signal regions, obtained before the final selections on this quantity (but after applying all other selections), for data and the different MC samples normalized with the theoretical cross-sections, i.e. before applying the normalization from the CR fit, are shown in Figure 7. Similarly, distributions of the final discriminant variables used in the RJR-based search, $H_{\text{T 2,1}}^{\text{PP}}$ ($H_{\text{T 4,1}}^{\text{PP}}$ where appropriate) in selected RJR-S and RJR-G regions, and $p_{\text{TS}}^{\text{CM}}$ in selected RJR-C regions, after applying all other selection requirements except those based on the plotted variable, before applying the normalization from the CR fit, are shown in Figure 8. Examples of typical expected SUSY signals are shown for illustration. These signals correspond to the processes to which each SR is primarily sensitive – $\tilde{q}\tilde{q}$ production for the lower jet-multiplicity SRs and $\tilde{g}\tilde{g}$ production for the higher jet-multiplicity SRs. In these figures, data and background distributions largely agree within uncertainties.

In the absence of a statistically significant excess, limits are set on contributions to the SRs from BSM physics. Upper limits at 95% CL on the number of BSM signal events in each SR and the corresponding visible BSM cross-section are derived from the model-independent fits described in Section 6 using the CL_{s} prescription. Limits are evaluated using MC pseudo-experiments. The results are presented in Tables 7 and 8.

The model-dependent fits in all the SRs are then used to set limits on specific classes of SUSY models. Two searches presented in this document are combined such that the final combined observed and expected 95% CL exclusion limits are obtained from the signal regions with the best expected CL_{s} value.

In Figure 9, limits are shown for two classes of simplified models in which only direct production of light-flavour squark or gluino pairs are considered. Limits are obtained by using the signal region with the best expected sensitivity at each point. In these simplified model scenarios, the upper limit of the excluded light-flavour squark mass region is 1.35 TeV assuming massless $\tilde{\chi}_1^0$, as obtained from the signal region RJR-S3b. The corresponding limit on the gluino mass is 1.86 TeV if the $\tilde{\chi}_1^0$ is massless, as obtained from the signal region Meff-4j-2600. The best sensitivity in the region of parameter space where the mass difference between the squark (gluino) and the lightest neutralino is small, is obtained from the dedicated RJR-C signal regions. In these regions with very compressed spectra with mass difference < 10 GeV, squark (gluino) masses up to 600 GeV (850 GeV) are excluded.

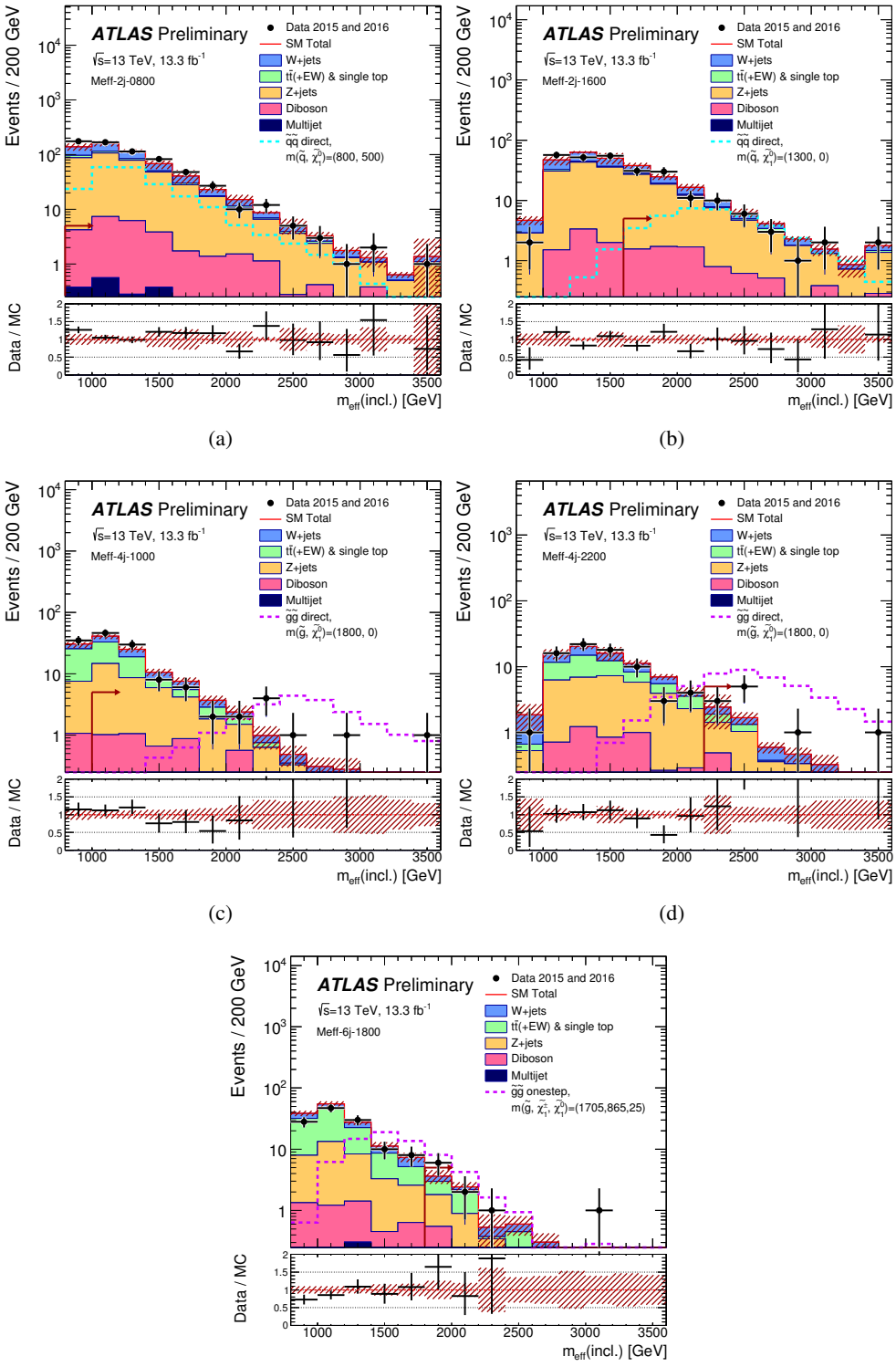

Figure 7: Observed m_{eff}(incl.) distributions for the (a) Meff-2j-0800, (b) Meff-2j-1600, (c) Meff-4j-1000, (d) Meff-4j-2200 and (e) Meff-6j-1800 signal regions. The histograms denote the MC background expectations prior to the fits described in the text, normalized to cross-section times integrated luminosity. The last bin includes the overflow. The hatched (red) error bands denote the combined experimental, MC statistical and theoretical modelling uncertainties. The arrows indicate the values at which the requirements on m_{eff}(incl.) are applied. Expected distributions for benchmark model points, normalized to NLO+NLL cross-section (Section 3) times integrated luminosity, are also shown for comparison (masses in GeV).

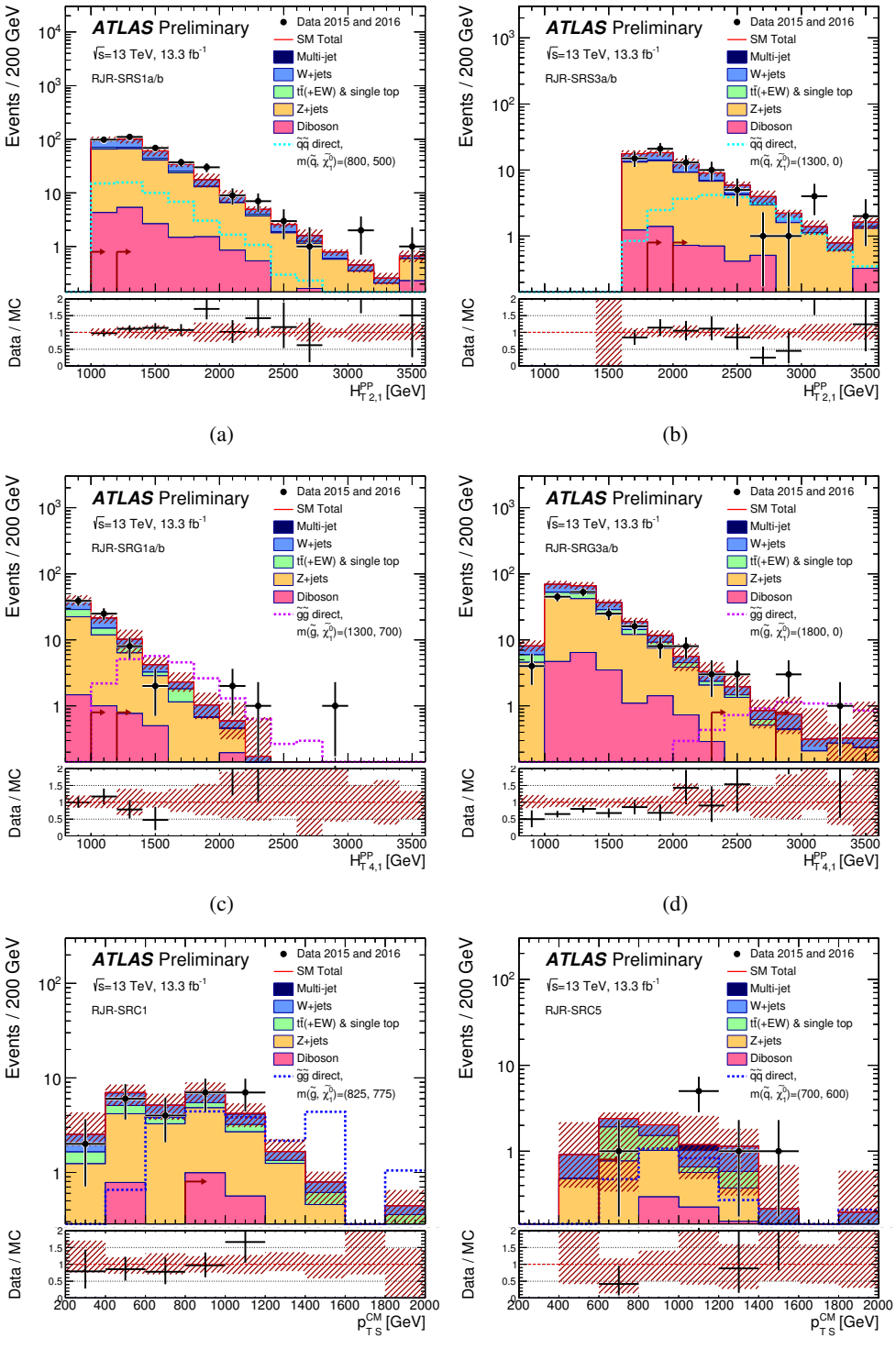

Figure 8: Observed $H_{\mathrm{T}\,2,1}^{\mathrm{PP}}$ distributions for the (a) RJR-S1a/b and (b) RJR-S3a/b signal regions, $H_{\mathrm{T}\,4,1}^{\mathrm{PP}}$ distributions for the (c) RJR-G1a/b and (d) RJR-G3a/b signal regions, and $p_{\mathrm{TS}}^{\mathrm{CM}}$ distributions for the (e) RJR-C1 and (f) RJR-C5 signal regions, after applying all selection requirements except those on the plotted variable. The histograms denote the MC background expectations prior to the fits described in the text, normalized to cross-section times integrated luminosity. The last bin includes the overflow. The hatched (red) error bands denote the combined experimental, MC statistical and theoretical modelling uncertainties. The arrows indicate the values at which the requirements on the plotted variable are applied. When two arrows are shown, these correspond to the looser SR variation 'a' and the tighter variation 'b'. Expected distributions for benchmark model points, normalized to NLO+NLL cross-section (Section 3) times integrated luminosity, are also shown for comparison (masses in GeV).

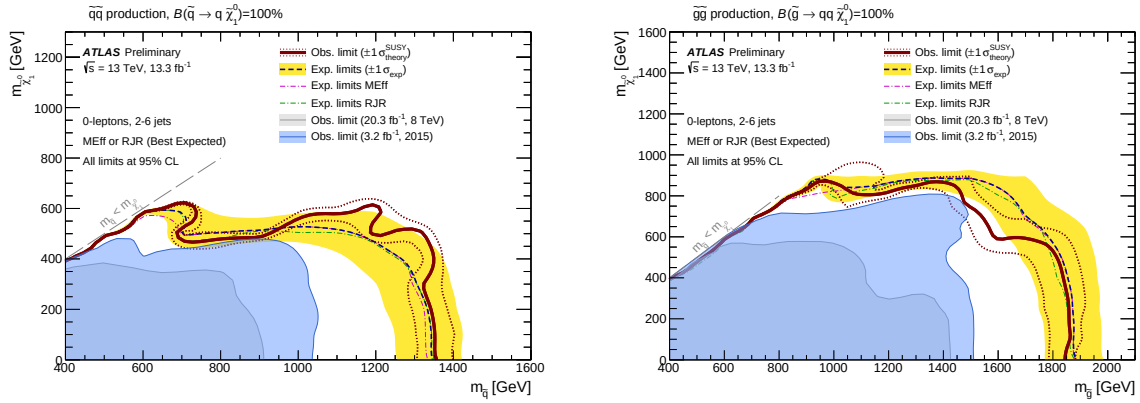

(a) (b)

Figure 9: Exclusion limits for direct production of (a) light-flavour squark pairs with decoupled gluinos and (b) gluino pairs with decoupled squarks. Gluinos (light-flavour squarks) are required to decay to two quarks (one quark) and a neutralino LSP. Exclusion limits are obtained by using the signal region with the best expected sensitivity at each point. Expected limits from the Meff- and RJR-based searches separately are also shown for comparison. The blue dashed lines show the expected limits at 95% CL, with the light (yellow) bands indicating the 1σ excursions due to experimental and background-only theoretical uncertainties. Observed limits are indicated by medium dark (maroon) curves where the solid contour represents the nominal limit, and the dotted lines are obtained by varying the signal cross-section by the renormalization and factorization scale and PDF uncertainties. Results are compared with the observed limits obtained by the previous ATLAS searches with no leptons, jets and missing transverse momentum [11, 16].

In Figure 10, limits are shown for pair-produced gluinos each decaying via an intermediate $\tilde{\chi}_1^\pm$ to two quarks, a W boson and a $\tilde{\chi}_1^0$, or via an intermediate $\tilde{\chi}_2^0$ to two quarks, a Z boson and a $\tilde{\chi}_1^0$. Results in Figure 10(a) are presented for simplified models in which the mass of the chargino $\tilde{\chi}_1^\pm$ is fixed to $m(\tilde{\chi}_1^\pm) = (m(\tilde{g}) + m(\tilde{\chi}_1^0))/2$. For a $\tilde{\chi}_1^0$ mass up to $\sim$ 400 GeV, the lower limit on the gluino mass, obtained from the signal region Meff-6j-2200, extends up to 1.83 TeV in this model. In the region of parameter space where the mass difference between the gluino and the lightest neutralino is small, the best sensitivity is obtained from the signal region Meff-3j-1200. In Figure 10(b) results are presented in $(m_{\tilde{\chi}_2^0}, m_{\tilde{g}})$ plane, and the mass of the $\tilde{\chi}_1^0$ is set to 1 GeV. In these models, gluino masses below 1.9 TeV are excluded for $\tilde{\chi}_2^0$ masses of $\sim$ 600 GeV as obtained from the signal region Meff-4j-2600.

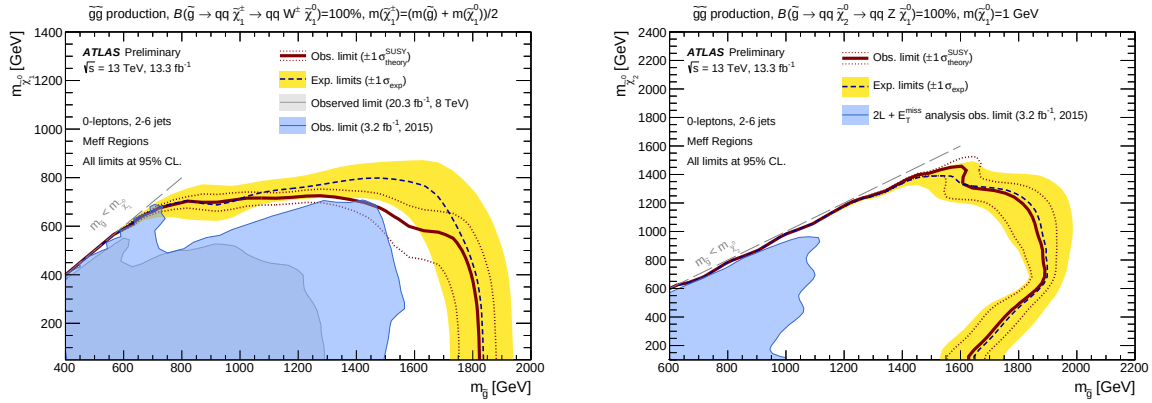

(a) (b)

Figure 10: Exclusion limits for pair-produced gluinos each decaying via an intermediate (a) $\tilde{\chi}_1^{\pm}$ to two quarks, a W boson and a $\tilde{\chi}_1^0$ for models with a fixed $m(\tilde{\chi}_1^{\pm}) = (m(\tilde{g}) + m(\tilde{\chi}_1^0))/2$ and varying values of $m(\tilde{g})$ and $m(\tilde{\chi}_1^0)$ and (b) $\tilde{\chi}_2^0$ to two quarks, a Z boson and a $\tilde{\chi}_1^0$ for models with a fixed $m(\tilde{\chi}_1^0) = 1$ GeV and varying values of $m(\tilde{g})$ and $m(\tilde{\chi}_2^0)$. Exclusion limits are obtained by using the signal region with the best expected sensitivity at each point. The blue dashed lines show the expected limits at 95% CL, with the light (yellow) bands indicating the 1σ excursions due to experimental and background-only theoretical uncertainties. Observed limits are indicated by medium dark (maroon) curves where the solid contour represents the nominal limit, and the dotted lines are obtained by varying the signal cross-section by the renormalization and factorization scale and PDF uncertainties. Results (a) are compared with the observed limits obtained by the previous ATLAS searches with no leptons, jets and missing transverse momentum [11, 16]. Results (b) are compared with the observed limits obtained by the previous ATLAS search in events containing a leptonically decaying Z boson, jets and missing transverse momentum [98].

11. Conclusion

This document presents results of the two selection strategies to search for squarks and gluinos in final states containing high-p_{T} jets, large missing transverse momentum but no electrons or muons, based on a 13.3 fb^{-1} dataset of $\sqrt{s} = 13$ TeV proton–proton collisions recorded by the ATLAS experiment at the LHC in 2015 and 2016.

Results are interpreted in terms of simplified models with only light-flavour squarks, or gluinos, together with a neutralino LSP, with the masses of all the other SUSY particles set beyond the reach of the LHC. For a massless lightest neutralino, gluino masses below 1.86 TeV are excluded at the 95% confidence level in a simplified model with only gluinos and the lightest neutralino. For a simplified model involving the strong production of squarks of the first and second generations, with decays to a massless lightest neutralino, squark masses below 1.35 TeV are excluded, assuming mass-degenerate squarks. In simplified models with pair-produced gluinos, each decaying via an intermediate $\tilde{\chi}_1^{\pm}$ to two quarks, a W boson and a $\tilde{\chi}_1^0$, gluino masses below 1.83 TeV are excluded for $\tilde{\chi}_1^0$ masses up to ~ 400 GeV. In simplified models with pair-produced gluinos, each decaying via an intermediate $\tilde{\chi}_2^0$ to two quarks, a Z boson and a $\tilde{\chi}_1^0$, gluino masses of at least 1.65 TeV are excluded for $\tilde{\chi}_2^0$ masses less than 1.2 TeV, and gluino mass limit reaches 1.9 TeV for $\tilde{\chi}_2^0$ masses of ~ 600 GeV. These results substantially extend the region of supersymmetric parameter space excluded by previous LHC searches.

Appendix

A. Signal regions providing the best expected sensitivity per model point

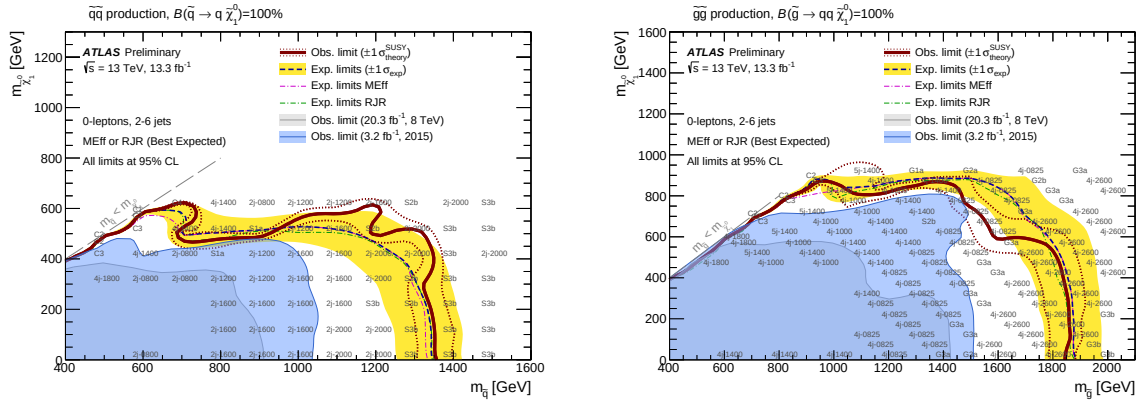

(a) (b)

Figure 11: Exclusion limits for direct production of (a) light-flavour squark pairs with decoupled gluinos and (b) gluino pairs with decoupled squarks. Gluinos (light-flavour squarks) are required to decay to two quarks (one quark) and a neutralino LSP. Exclusion limits are obtained by using the signal region with the best expected sensitivity at each point. The signal regions providing the best expected sensitivity at a selection of model points are indicated. The blue dashed lines show the expected limits at 95% CL, with the light (yellow) bands indicating the 1σ excursions due to experimental and background-only theoretical uncertainties. Observed limits are indicated by medium dark (maroon) curves where the solid contour represents the nominal limit, and the dotted lines are obtained by varying the signal cross-section by the renormalization and factorization scale and PDF uncertainties. Results are compared with the observed limits obtained by the previous ATLAS searches with no leptons, jets and missing transverse momentum [11, 16].

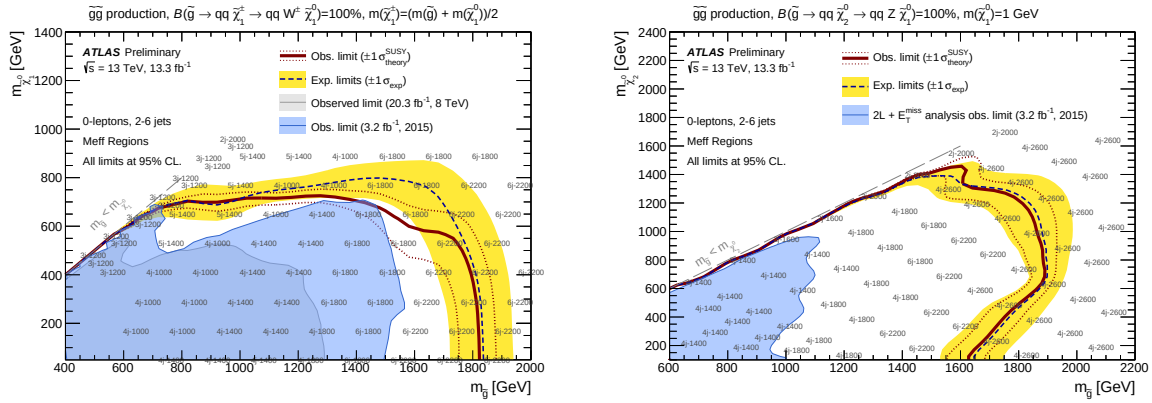

(a) (b)

Figure 12: Exclusion limits for pair-produced gluinos each decaying via an intermediate (a) $\tilde{\chi}_1^{\pm}$ to two quarks, a W boson and a $\tilde{\chi}_1^0$ for models with a fixed $m(\tilde{\chi}_1^{\pm}) = (m(\tilde{g}) + m(\tilde{\chi}_1^0))/2$ and varying values of $m(\tilde{g})$ and $m(\tilde{\chi}_1^0)$ and (b) $\tilde{\chi}_2^0$ to two quarks, a Z boson and a $\tilde{\chi}_1^0$ for models with a fixed $m(\tilde{\chi}_1^0) = 1$ GeV and varying values of $m(\tilde{g})$ and $m(\tilde{\chi}_2^0)$. Exclusion limits are obtained by using the signal region with the best expected sensitivity at each point. The signal regions providing the best expected sensitivity at a selection of model points are indicated. The blue dashed lines show the expected limits at 95% CL, with the light (yellow) bands indicating the 1σ excursions due to experimental and background-only theoretical uncertainties. Observed limits are indicated by medium dark (maroon) curves where the solid contour represents the nominal limit, and the dotted lines are obtained by varying the signal cross-section by the renormalization and factorization scale and PDF uncertainties. Results (a) are compared with the observed limits obtained by the previous ATLAS searches with no leptons, jets and missing transverse momentum [11, 16]. Results (b) are compared with the observed limits obtained by the previous ATLAS search in events containing a leptonically decaying Z boson, jets and missing transverse momentum [98].

References

[1] Y. A. Golfand and E. P. Likhtman, *Extension of the Algebra of Poincare Group Generators and Violation of p Invariance*, JETP Lett. **13** (1971) 323, [Pisma Zh.Eksp.Teor.Fiz.13:452-455,1971].

[2] D. V. Volkov and V. P. Akulov, *Is the Neutrino a Goldstone Particle?*, Phys. Lett. B **46** (1973) 109.

[3] J. Wess and B. Zumino, *Supergauge Transformations in Four-Dimensions*, Nucl. Phys. B **70** (1974) 39.

[4] J. Wess and B. Zumino, *Supergauge Invariant Extension of Quantum Electrodynamics*, Nucl. Phys. B **78** (1974) 1.

[5] S. Ferrara and B. Zumino, *Supergauge Invariant Yang-Mills Theories*, Nucl. Phys. B **79** (1974) 413.

[6] A. Salam and J. A. Strathdee, *Supersymmetry and Nonabelian Gauges*, Phys. Lett. B **51** (1974) 353.

[7] G. R. Farrar and P. Fayet, *Phenomenology of the Production, Decay, and Detection of New Hadronic States Associated with Supersymmetry*, Phys. Lett. B **76** (1978) 575.

[8] L. Evans and P. Bryant, *LHC Machine*, JINST **3** (2008) S08001.

[9] P. Fayet, *Supersymmetry and Weak, Electromagnetic and Strong Interactions*, Phys. Lett. B **64** (1976) 159.

[10] P. Fayet, *Spontaneously Broken Supersymmetric Theories of Weak, Electromagnetic and Strong Interactions*, Phys. Lett. B **69** (1977) 489.

[11] ATLAS Collaboration, *Search for squarks and gluinos in final states with jets and missing transverse momentum at $\sqrt{s}$ = 13 TeV with the ATLAS detector*, Submitted to EPJC (2016), arXiv: 1605.03814 [hep-ex].

[12] P. Jackson, C. Rogan and M. Santoni, *Sparticles in Motion - getting to the line in compressed scenarios with the Recursive Jigsaw Reconstruction*, (2016), arXiv: 1607.08307 [hep-ph].

[13] ATLAS Collaboration, *Search for squarks and gluinos using final states with jets and missing transverse momentum with the ATLAS detector in $\sqrt{s}$ = 7 TeV proton-proton collisions*, Phys. Lett. B **701** (2011) 186, arXiv: 1102.5290 [hep-ex].

[14] ATLAS Collaboration, *Search for squarks and gluinos using final states with jets and missing transverse momentum with the ATLAS detector in $\sqrt{s}$ = 7 TeV proton-proton collisions*, Phys. Lett. B **710** (2012) 67, arXiv: 1109.6572 [hep-ex].

[15] ATLAS Collaboration, *Search for squarks and gluinos with the ATLAS detector in final states with jets and missing transverse momentum using 4.7 fb^{-1} of $\sqrt{s}$ = 7 TeV proton-proton collision data*, Phys. Rev. D **87** (2013) 012008, arXiv: 1208.0949 [hep-ex].

[16] ATLAS Collaboration, *Search for squarks and gluinos with the ATLAS detector in final states with jets and missing transverse momentum using $\sqrt{s}$ = 8 TeV proton–proton collision data*, JHEP **09** (2014) 176, arXiv: 1405.7875 [hep-ex].

[17] ATLAS Collaboration, *Summary of the searches for squarks and gluinos using $\sqrt{s}$ = 8 TeV pp collisions with the ATLAS experiment at the LHC*, JHEP **10** (2015) 054, arXiv: 1507.05525 [hep-ex].

[18] CMS Collaboration, *Search for supersymmetry in hadronic final states using MT2 in pp collisions at $\sqrt{s}$ = 7 TeV*, JHEP **10** (2012) 018, arXiv: 1207.1798 [hep-ex].

[19] CMS Collaboration, *Search for new physics in the multijet and missing transverse momentum final state in proton-proton collisions at $\sqrt{s}$ = 7 TeV*, Phys. Rev. Lett. **109** (2012) 171803, arXiv: 1207.1898 [hep-ex].

[20] CMS Collaboration, *Search for supersymmetry in hadronic final states with missing transverse energy using the variables α_{T} and b-quark multiplicity in pp collisions at 8 TeV*, Eur. Phys. J. C **73** (2013) 2568, arXiv: 1303.2985 [hep-ex].

[21] CMS Collaboration, *Inclusive search for supersymmetry using the razor variables in pp collisions at $\sqrt{s}$ = 7 TeV*, Phys. Rev. Lett. **111** (2013) 081802, arXiv: 1212.6961 [hep-ex].

[22] CMS Collaboration, *Search for new physics in the multijet and missing transverse momentum final state in proton-proton collisions at $\sqrt{s}$= 8 TeV*, JHEP **06** (2014) 055, arXiv: 1402.4770 [hep-ex].

[23] CMS Collaboration, *Searches for Supersymmetry using the M_{T2} Variable in Hadronic Events Produced in pp Collisions at 8 TeV*, JHEP **05** (2015) 078, arXiv: 1502.04358 [hep-ex].

[24] CMS Collaboration, *Search for new physics in final states with jets and missing transverse momentum in $\sqrt{s}$ = 13 TeV pp collisions with the α_T variable*, CMS-PAS-SUS-15-005 (2015), URL: http://inspirehep.net/record/1410157.

[25] CMS Collaboration, *Inclusive search for supersymmetry using the razor variables at sqrt(s) = 13 TeV*, CMS-PAS-SUS-15-004 (2015), URL: https://cds.cern.ch/record/2114815.

[26] CMS Collaboration, *Search for new physics with the MT2 variable in all-jets final states produced in pp collisions at sqrt(s) = 13 TeV*, Submitted to JHEP (2016), arXiv: 1603.04053 [hep-ex].

[27] ATLAS Collaboration, *Search for gluinos in events with an isolated lepton, jets and missing transverse momentum at $\sqrt{s}$ = 13 TeV with the ATLAS detector*, Submitted to EPJC (2016), arXiv: 1605.04285 [hep-ex].

[28] J. Alwall et al., *Searching for Directly Decaying Gluinos at the Tevatron*, Phys. Lett. B **666** (2008) 34, arXiv: 0803.0019 [hep-ph].

[29] J. Alwall, P. Schuster and N. Toro, *Simplified Models for a First Characterization of New Physics at the LHC*, Phys. Rev. D **79** (2009) 075020, arXiv: 0810.3921 [hep-ph].

[30] D. Alves et al., *Simplified Models for LHC New Physics Searches*, J. Phys. G: Nucl. Part. Phys. **39** (2012) 105005, arXiv: 1105.2838 [hep-ph].

[31] ATLAS Collaboration, *The ATLAS Experiment at the CERN Large Hadron Collider*, JINST **3** (2008) S08003.

[32] ATLAS Collaboration, *ATLAS Insertable B-Layer Technical Design Report*, ATLAS-TDR-19 (2010), URL: http://cdsweb.cern.ch/record/1291633.

[33] ATLAS Collaboration, *Performance of the ATLAS Trigger System in 2010*, Eur. Phys. J. C **72** (2012) 1849, arXiv: 1110.1530 [hep-ex].

[34] ATLAS Collaboration, *2015 start-up trigger menu and initial performance assessment of the ATLAS trigger using Run-2 data*, ATL-DAQ-PUB-2016-001 (2016), URL: https://cds.cern.ch/record/2104298.

[35] ATLAS Collaboration, *Improved luminosity determination in pp collisions at $\sqrt{s}$ = 7 TeV using the ATLAS detector at the LHC*, Eur. Phys. J. C **73** (2013) 2518, arXiv: 1302.4393 [hep-ex].

[36] J. Alwall, R. Frederix, S. Frixione, V. Hirschi, F. Maltoni, O. Mattelaer, H. -S. Shao, T. Stelzer, P. Torrielli, M. Zaro, *The automated computation of tree-level and next-to-leading order differential cross sections, and their matching to parton shower simulations*, JHEP **07** (2014) 079, arXiv: 1405.0301 [hep-ph].

[37] T. Sjöstrand et al., *An Introduction to PYTHIA 8.2*, Comput. Phys. Commun. **191** (2015) 159, arXiv: 1410.3012 [hep-ph].

[38] L. Lönnblad and S. Prestel, *Matching Tree-Level Matrix Elements with Interleaved Showers*, JHEP **03** (2012) 019, arXiv: 1109.4829 [hep-ph].

[39] ATLAS Collaboration, *Summary of ATLAS Pythia 8 tunes*, ATL-PHYS-PUB-2012-003 (2012), URL: http://cdsweb.cern.ch/record/1474107.

[40] R. D. Ball et al., *Parton distributions with LHC data*, Nucl. Phys. B **867** (2013) 244, arXiv: 1207.1303 [hep-ph].

[41] D. J. Lange, *The EvtGen particle decay simulation package*, Nucl. Instrum. Meth. A **462** (2001) 152.

[42] T. Gleisberg et al., *Event generation with SHERPA 1.1*, JHEP **02** (2009) 007, arXiv: 0811.4622 [hep-ph].

[43] W. Beenakker et al., *Squark and gluino production at hadron colliders*, Nucl. Phys. B **492** (1997) 51, arXiv: hep-ph/9610490.

[44] A. Kulesza and L. Motyka, *Threshold resummation for squark-antisquark and gluino-pair production at the LHC*, Phys. Rev. Lett. **102** (2009) 111802, arXiv: 0807.2405 [hep-ph].

[45] A. Kulesza and L. Motyka, *Soft gluon resummation for the production of gluino-gluino and squark-antisquark pairs at the LHC*, Phys. Rev. D **80** (2009) 095004, arXiv: 0905.4749 [hep-ph].

[46] W. Beenakker et al., *Soft-gluon resummation for squark and gluino hadroproduction*, JHEP **12** (2009) 041, arXiv: 0909.4418 [hep-ph].

[47] W. Beenakker et al., *Squark and gluino hadroproduction*, Int. J. Mod. Phys. A **26** (2011) 2637, arXiv: 1105.1110 [hep-ph].

[48] M. Krämer et al., *Supersymmetry production cross sections in pp collisions at* $\sqrt{s} = 7$ *TeV*, (), arXiv: 1206.2892 [hep-ph].

[49] ATLAS Collaboration, *Monte Carlo Generators for the Production of a W or* Z/γ^* *Boson in Association with Jets at ATLAS in Run 2*, ATL-PHYS-PUB-2016-003 (2016), URL: http://cds.cern.ch/record/2120133.

[50] T. Gleisberg and S. Höche, *Comix, a new matrix element generator*, JHEP **12** (2008) 039, arXiv: 0808.3674 [hep-ph].

[51] F. Cascioli, P. Maierhofer and S. Pozzorini, *Scattering Amplitudes with Open Loops*, Phys. Rev. Lett. **108** (2012) 111601, arXiv: 1111.5206 [hep-ph].

[52] S. Schumann and F. Krauss, *A Parton shower algorithm based on Catani-Seymour dipole factorisation*, JHEP **03** (2008) 038, arXiv: 0709.1027 [hep-ph].

[53] S. Höche et al., *QCD matrix elements + parton showers: The NLO case*, JHEP **04** (2013) 027, arXiv: 1207.5030 [hep-ph].

[54] S. Höche, F. Krauss, S. Schumann and F. Siegert, *QCD matrix elements and truncated showers*, JHEP **05** (2009) 053, arXiv: 0903.1219 [hep-ph].

[55] R. D. Ball et al., *Parton distributions for the LHC Run II*, JHEP **04** (2015) 040, arXiv: 1410.8849 [hep-ph].

[56] H.-L. Lai et al., *New parton distributions for collider physics*, Phys. Rev. D **82** (2010) 074024, arXiv: 1007.2241 [hep-ph].

[57] F. P. R. Gavin Y. Li and S. Quackenbush, *FEWZ 2.0: A code for hadronic Z production at next-to-next-to-leading order*, Comput. Phys. Commun. **182** (2011) 2388, arXiv: 1011.3540 [hep-ph].

[58] ATLAS Collaboration, *Simulation of top quark production for the ATLAS experiment at* $\sqrt{s}$ = 13 TeV, ATL-PHYS-PUB-2016-004 (2016), URL: http://cds.cern.ch/record/2120417.

[59] S. Alioli et al., *A general framework for implementing NLO calculations in shower Monte Carlo programs: the POWHEG BOX*, JHEP **06** (2010) 043, arXiv: 1002.2581 [hep-ph].

[60] P. Artoisenet et al., *Automatic spin-entangled decays of heavy resonances in Monte Carlo simulations*, JHEP **03** (2013) 015, arXiv: 1212.3460 [hep-ph].

[61] T. Sjöstrand, S. Mrenna and P. Skands, *PYTHIA 6.4 Physics and Manual*, JHEP **05** (2006) 026, arXiv: hep-ph/0603175.

[62] J. Pumplin et al., *New generation of parton distributions with uncertainties from global QCD analysis*, JHEP **07** (2002) 012, arXiv: hep-ph/0201195 [hep-ph].

[63] P. Z. Skands, *Tuning Monte Carlo Generators: The Perugia Tunes*, Phys. Rev. D **82** (2010) 074018, arXiv: 1005.3457 [hep-ph].

[64] M. Czakon, P. Fiedler and A. Mitov, *Total Top-Quark Pair-Production Cross Section at Hadron Colliders Through* $O(\alpha_S^4)$, Phys. Rev. Lett. **110** (2013) 252004, arXiv: 1303.6254 [hep-ph].

[65] M. Czakon and A. Mitov, *Top++: A Program for the Calculation of the Top-Pair Cross-Section at Hadron Colliders*, Comput. Phys. Commun. **185** (2014) 2930, arXiv: 1112.5675 [hep-ph].

[66] M. Aliev et al., *HATHOR: HAdronic Top and Heavy quarks crOss section calculatoR*, Comput. Phys. Commun. **182** (2011) 1034, arXiv: 1007.1327 [hep-ph].

[67] P. Kant et al., *HatHor for single top-quark production: Updated predictions and uncertainty estimates for single top-quark production in hadronic collisions*, Comput. Phys. Commun. **191** (2015) 74, arXiv: 1406.4403 [hep-ph].

[68] N. Kidonakis, *Two-loop soft anomalous dimensions for single top quark associated production with a W- or H-*, Phys. Rev. D **82** (2010) 054018, arXiv: 1005.4451 [hep-ph].

[69] N. Kidonakis, *Next-to-next-to-leading-order collinear and soft gluon corrections for t-channel single top quark production*, Phys. Rev. D **83** (2011) 091503, arXiv: 1103.2792 [hep-ph].

[70] ATLAS Collaboration, *Modelling of the $t\bar{t}H$ and $t\bar{t}V$ ($V = W, Z$) processes for $\sqrt{s} = 13$ TeV ATLAS analyses*, ATL-PHYS-PUB-2016-005 (2016), URL: http://cds.cern.ch/record/2120826.

[71] K. M. A. Lazopoulos T. McElmurry and F. Petriello, *Next-to-leading order QCD corrections to $t\bar{t}Z$ production at the LHC*, Phys. Lett. B **666** (2008) 62, arXiv: 0804.2220 [hep-ph].

[72] J. M. Campbell and R. K. Ellis, *$t\bar{t}W^{\pm}$ production and decay at NLO*, JHEP **07** (2012) 052, arXiv: 1204.5678 [hep-ph].

[73] ATLAS Collaboration, *Multi-Boson Simulation for 13 TeV ATLAS Analyses*, ATL-PHYS-PUB-2016-002 (2016), URL: http://cds.cern.ch/record/2119986.

[74] ATLAS Collaboration, *The ATLAS Simulation Infrastructure*, Eur. Phys. J. C **70** (2010) 823, arXiv: 1005.4568 [physics.ins-det].

[75] S. Agostinelli et al., *GEANT4: A simulation toolkit*, Nucl. Instrum. Meth. A **506** (2003) 250.

[76] ATLAS Collaboration, *The simulation principle and performance of the ATLAS fast calorimeter simulation FastCaloSim*, ATL-PHYS-PUB-2010-013 (2010), URL: http://cds.cern.ch/record/1300517.

[77] A. D. Martin, W. J. Stirling, R. S. Thorne, G. Watt, *Parton distributions for the LHC*, Eur. Phys. J. C **63** (2009) 189, arXiv: 0901.0002 [hep-ph].

[78] M. Cacciari, G. P. Salam and G. Soyez, *The anti-k_t jet clustering algorithm*, JHEP **04** (2008) 063, arXiv: 0802.1189 [hep-ph].

[79] M. Cacciari and G. P. Salam, *Dispelling the N^3 myth for the k_t jet-finder*, Phys. Lett. B **641** (2006) 57, arXiv: hep-ph/0512210.

[80] W. Lampl et al., *Calorimeter Clustering Algorithms: Description and Performance*, (2008), URL: http://cdsweb.cern.ch/record/1099735.

[81] M. Cacciari and G. P. Salam, *Pileup subtraction using jet areas*, Phys. Lett. B **659** (2008) 119, arXiv: 0707.1378 [hep-ph].

[82] ATLAS Collaboration, *Performance of pile-up mitigation techniques for jets in pp collisions at $\sqrt{s} = 8$ TeV using the ATLAS detector*, Submitted to EPJC (2015), arXiv: 1510.03823 [hep-ex].

[83] ATLAS Collaboration, *Jet Calibration and Systematic Uncertainties for Jets Reconstructed in the ATLAS Detector at $\sqrt{s} = 13$ TeV*, ATL-PHYS-PUB-2015-015 (2015), URL: http://cdsweb.cern.ch/record/2037613.

[84] G. Aad et al., *Performance of b-Jet Identification in the ATLAS Experiment*, JINST **11** (2016) P04008, arXiv: 1512.01094 [hep-ex].

[85] ATLAS Collaboration, *Optimisation of the ATLAS b-tagging performance for the 2016 LHC Run*, ATL-PHYS-PUB-2016-012 (2016), URL: https://cds.cern.ch/record/2160731.

[86] ATLAS Collaboration, *Selection of jets produced in proton-proton collisions with the ATLAS detector using 2015 data*, ATLAS-CONF-2015-029 (2015), URL: http://cdsweb.cern.ch/record/2037702.

[87] ATLAS Collaboration, *Tagging and suppression of pileup jets with the ATLAS detector*, ATLAS-CONF-2014-018 (2014), URL: http://cds.cern.ch/record/1700870.

[88] ATLAS Collaboration, *Muon reconstruction performance of the ATLAS detector in proton?proton collision data at $\sqrt{s}$ =13 TeV*, Eur. Phys. J. **C76** (2016) 292, arXiv: 1603.05598 [hep-ex].

[89] ATLAS Collaboration, *Electron identification measurements in ATLAS using $\sqrt{s}$ = 13 TeV data with 50 ns bunch spacing*, ATL-PHYS-PUB-2015-041 (2015), URL: http://cdsweb.cern.ch/record/2048202.

[90] ATLAS Collaboration, *Expected performance of missing transverse momentum reconstruction for the ATLAS detector at $\sqrt{s}$ = 13 TeV*, ATL-PHYS-PUB-2015-023 (2015), URL: http://cdsweb.cern.ch/record/2037700.

[91] ATLAS Collaboration, *Measurements of the Photon Identification Efficiency with the ATLAS Detector using 4.9 fb^{-1} of pp Collision Data Collected in 2011*, ATLAS-CONF-2012-123 (2012), URL: http://cdsweb.cern.ch/record/1473426.

[92] M. Baak et al., *HistFitter software framework for statistical data analysis*, Eur. Phys. J. C **75** (2015) 153, arXiv: 1410.1280 [hep-ex].

[93] A. L. Read, *Presentation of Search Results: The CL(s) Technique*, J. Phys. G **28** (2002) 2693.

[94] C. Chen, *New approach to identifying boosted hadronically decaying particles using jet substructure in its center-of-mass frame*, Phys. Rev. D **85** (2012) 034007, arXiv: 1112.2567 [hep-ph].

[95] ATLAS Collaboration, *Jet energy measurement with the ATLAS detector in proton-proton collisions at $\sqrt{s}$ = 7 TeV*, Eur. Phys. J. C **73** (2013) 2304, arXiv: 1112.6426 [hep-ex].

[96] ATLAS Collaboration, *Single hadron response measurement and calorimeter jet energy scale uncertainty with the ATLAS detector at the LHC*, Eur. Phys. J. C **73** (2013) 2305, arXiv: 1203.1302 [hep-ex].

[97] ATLAS Collaboration, *Jet energy resolution in proton-proton collisions at $\sqrt{s}$ = 7 TeV recorded in 2010 with the ATLAS detector*, Eur. Phys. J. C **73** (2013) 2306, arXiv: 1210.6210 [hep-ex].

[98] ATLAS Collaboration, *A search for Supersymmetry in events containing a leptonically decaying Z boson, jets and missing transverse momentum in $\sqrt{s}$ = 13 TeV pp collisions with the ATLAS detector*, ATLAS-CONF-2015-082 (2015), URL: http://cds.cern.ch/record/2114854.